

Politecnico di Torino

Politecnico di Torino

Master's Degree in Mechatronics Engineering

A.Y. 2025/2026

Graduation Session September 2026

Toward Compliant Legged Locomotion: Design and HASEL Soft-Actuator Integration of a Quasi-Passive Bipedal Walker

Supervisors:

Ph.D. Pangcheng David Cen Cheng

Prof. Alexandre Pitti

Candidate:

Francesco Bighiani

Summary

Rigid, position-controlled actuators resist external disturbances rather than yielding to them, which makes them poorly suited to the kind of compliant, adaptive interaction that biological systems achieve through muscles and tendons. This thesis investigates whether HASEL (Hydraulically Amplified Self-healing Electrostatic) soft actuators, a class of electrohydraulic actuators with muscle-like, intrinsically compliant behavior, can be used to drive a quasi-passive bipedal walking robot, as a step toward bio-inspired joints that rely on small, compliant corrective motions rather than rigid, high-torque actuation to stabilize legged locomotion. All experimental results reported in this thesis were obtained on physical hardware in a laboratory setting. MuJoCo was used only during the preliminary SO-101 phase for kinematic modeling and visualization; no simulation-based results were used to validate the walker or the HASEL integration. Prototypes were built, instrumented, and tested on the bench and, for the walker, on flat indoor and outdoor floor surfaces.

The work began with preliminary experiments on a LeRobot SO-101 robotic arm, exploring orientation-based postural stabilization and interaction-aware compliance on position-controlled hardware. These showed that stabilizing behavior can be approximated through active control, but only as an *apparent* form of compliance, fundamentally limited by the servo's internal position loop. This phase did not directly inform the walker's design, but it usefully grounded the rest of the project in hands-on compliant-control practice.

The core of the thesis is a servo-driven quasi-passive walker, modeled after minimally actuated leg-extension designs from the literature and iteratively refined through mechanical redesign (hip-axis offset, foot padding, leg spacing) and a systematic frequency–amplitude characterization, identifying a repeatable stable-walking regime and a best-performing tested actuation frequency near 1.0 Hz.

HASEL integration was then pursued through a dedicated, reusable actuator interface and three successive transmission architectures: direct-drive, lever-based, and scissor-based amplification, each addressing a specific failure mode of its predecessor. The direct-drive concept was limited mainly by insufficient actuator displacement and by structural compliance. The two amplification mechanisms, however, were both defeated by friction generated by non-axial loading. In the lever, the lateral offset of the prismatic guide produced a parasitic moment and binding; in the scissor, gait-induced leg bending forced the guided mechanism into lateral contact and consumed much of the available displacement. The HASEL

actuator's limited force and stroke margin made these frictional losses decisive. The scissor mechanism nevertheless reproduced its intended 2:1 amplification on the bench before losing that performance once mounted on the real walker.

These results indicate that this class of HASEL actuator, in its current form, is not a practical primary actuator for this walker architecture. The actuator interface developed along the way is nonetheless proposed as a reusable contribution for future small-displacement HASEL applications, such as fine positioning or compliant posture correction, where loading can be kept close to axial and large forces are not required.

Acknowledgements

I would like to thank my supervisors: Prof. Alexandre Pitti, for his guidance throughout this thesis and for the opportunity to carry out this internship at the ETIS laboratory, and Ph.D. Pangcheng David Cen Cheng, for thoughtfully revising this thesis.

I am deeply grateful to my parents, Luisa and Virginio, for supporting me throughout university, to my grandmother Nina and to my brother Federico, for always believing in me.

To my beautiful girlfriend Rigona, for patience, support during the months abroad and for always being by my side.

Finally, to my Erasmus friends who shared the lab with me during this experience, Stefano, Flavia and Lorenzo, for making this time abroad memorable.

Table of Contents

List of Figures VIII

1 Introduction 1
- 1.1 Motivation . . . 2
- 1.2 Research questions . . . 2
- 1.3 Experimental robotic platforms . . . 3
- 1.4 Thesis structure . . . 3

2 Related Work 4
- 2.1 Compliance and Soft Robotics . . . 4
- 2.2 HASEL Actuators . . . 5
- 2.3 Passive-Dynamic and Quasi-Passive Walking . . . 6
- 2.4 Position vs. Torque/Impedance Control in Servo Actuators . . . 7
- 2.5 Summary . . . 7

3 Preliminary Exploration: The SO-101 Robotic Arm 9
- 3.1 Experimental Robotic Platform . . . 9
- 3.2 Actuation System . . . 10
- 3.3 Software Framework . . . 11
- 3.4 Integration of an Inertial Measurement Unit . . . 12
- 3.5 Preliminary Compliance Experiments . . . 13
- 3.6 IMU-Based Postural Stabilization Experiment . . . 13
  - 3.6.1 Objective . . . 13
  - 3.6.2 Control Architecture . . . 13
  - 3.6.3 IMU-Based Orientation Estimation . . . 14
  - 3.6.4 Interpretation as Apparent Stiffness . . . 15
  - 3.6.5 Software Architecture Considerations . . . 15
  - 3.6.6 Observed Limitations . . . 16
- 3.7 IMU + Effort-Based Elbow Compliance . . . 16
- 3.8 Intermediate Inverted-Pendulum Setup . . . 18
- 3.9 Additional Exploration: ROS 2-Based Behavior Control . . . 19
- 3.10 Summary . . . 20

4 Experimental Platform: A Quasi-Passive Walker 21
4.1 Design Rationale . . . 21
4.2 Mechanical Architecture . . . 21
4.3 Electronics and Power Distribution . . . 24
4.3.1 Simplicity of the Gait-Generation Code . . . 26
4.4 Crank–Connecting Rod Mechanism for Leg Extension . . . 27
4.5 Mechanical Redesign and Dynamic Stability Adjustments . . . 29
4.6 Experimental Tuning Phase . . . 30
4.6.1 Amplitude–Frequency Characterization . . . 30
4.6.2 Best Configuration . . . 31
4.6.3 Velocity Testing . . . 34
4.7 IMU-Based Feedback Attempts and Mechanical Optimization Priority 35
4.8 Summary . . . 36

5 HASEL Actuator Integration 37
5.1 Actuator Selection and Characterization . . . 37
5.2 The HASEL–Mechanism Interface . . . 39
5.2.1 Modular Mechanical Connection . . . 40
5.3 Direct-Drive Attempt . . . 42
5.4 Lever-Based Amplification Mechanism . . . 43
5.5 Scissor-Based Motion Amplification Mechanism . . . 45
5.5.1 Design . . . 45
5.5.2 Tolerance Calibration and Lateral Guide . . . 46
5.5.3 Experimental Evaluation . . . 48
5.5.4 Mechanical Interpretation . . . 52
5.6 Summary . . . 53

6 Discussion 54
6.1 From Rigid to Soft Actuation: What Carries Over . . . 54
6.2 Mechanical Lessons from Three Transmission Attempts . . . 54
6.3 HASEL Feasibility for This Walker Design . . . 55
6.4 The HASEL Interface as a Reusable Contribution . . . 55
6.5 Implications for HASEL Applications . . . 56
6.6 Answering the Research Questions . . . 56

7 Conclusion and Future Work 57
7.1 Conclusion . . . 57
7.2 Limitations . . . 58
7.3 Future Work . . . 58

A Control Software Listings 60

List of Figures

3.1 The LeRobot SO-101 robotic arm platform used for the preliminary experiments [11]. 10
3.2 Feetech STS3215 smart servomotor used to actuate the SO-101 arm [19]. 10
3.3 MuJoCo simulation environment used for kinematic modeling and visualization of the SO-101 arm. 12
3.4 Cascade control architecture. The outer loop uses IMU orientation feedback to modify the desired joint position, while the inner position-control loop is implemented by the servomotor's internal PID controller. 14
3.5 Experimental setup for the IMU-based postural stabilization and effort-based compliance experiments: the SO-101 arm with the MPU-6050 IMU and Arduino Mega interface visible on the desk. . . 17
3.6 SO-101 arm in the preliminary inverted-pendulum-like pose used for the balancing experiment. 18

4.1 Early CAD assembly of the quasi-passive walker. 23
4.2 The early walker prototype, actuated by the original crank–connecting rod mechanism described below, with the Arduino Mega controller visible on top. 24
4.3 Schematic of the electrical connections between the 5 V USB power bank, Arduino Mega with custom prototyping shield, and the two Feetech FR0115M leg servomotors. Servo power is distributed directly from the shared 5 V rail, while the two PWM control signals are routed independently from the Arduino. 25
4.4 Arduino Mega mounted on the custom prototyping shield used to distribute power to the walker's servomotors. The shield's JST connector (left, with red/black leads) connects to the 5 V USB power bank; PWM signal wires run separately to the servo headers, while power is distributed directly to the servos rather than through the Arduino's own regulator. 26
4.5 Close-up of the crank joint at the leg's actuation point, showing the servo mounting bracket and the crank arm connecting to the servo horn. 27

4.6 Kinematic diagram of the crank–connecting rod mechanism, with crank radius $r = 25.5$ mm, connecting rod length $l = 60$ mm, and crank angle θ measured from the vertical axis. 28
4.7 The two printed upper leg brackets side by side, before (17 mm) and after (13 mm) the hip-axis offset adjustment. 29
4.8 Walking performance as a function of actuation frequency and estimated real amplitude, without padded soles (left) and with padded soles (right). Color indicates qualitative walking score, ranging from 1 (no walking) to 4 (stable walking). 31
4.9 Walking performance map for the best-performing configuration: 13 mm hip offset, padded soles, 20 mm spacer. 32
4.10 The finished, servo-driven walker in its best-performing configuration (13 mm hip offset, padded soles, 20 mm spacer), the configuration used throughout the frequency–amplitude and velocity characterization presented in this chapter. 33
4.11 The finished walker during outdoor testing, viewed from the front (left) and from the side (right). 33
4.12 Walking speed as a function of actuation frequency, for the best configuration (13 mm hip offset, padded soles, 20 mm spacer), at two estimated real amplitudes. 34

5.1 The E-0025-04-15 HASEL actuator used in this study. Actuator parameters according to the manufacturer (blocking force, free displacement, dimensions, weight) [3]. 37
5.2 CAD render of the rigid HASEL–mechanism interface, showing the spring-loaded linear guides around the central actuator support. . . 39
5.3 The modular mounting interface: the standardized lower moving plate, with its central fastening screw and positioning pin, mounted on the 3D-printed leg (left); and the same connector in use, coupling the scissor-based transmission mechanism to the actuator interface (right). This connector geometry was reused unmodified across the direct-drive, lever-based, and scissor-based transmission mechanisms. 41
5.4 First direct-drive prototype coupling the HASEL actuator directly to the telescopic leg. 42
5.5 CAD design of the lever-based amplification mechanism with integrated prismatic guide. 44
5.6 Physical prototype of the lever-based amplification mechanism under manual testing. 45
5.7 CAD design of the scissor-based (pantograph) amplification mechanism. 46

5.8 Assembled scissor mechanism showing the added lateral guide rod (steel, same diameter as the scissor pivot pins) and nylon washer used to constrain out-of-plane deflection while minimizing additional sliding friction. 48
5.9 The scissor mechanism under stand-alone bench testing, used to measure the input/output displacement ratio under applied load. . 49
5.10 Output linear displacement of the stand-alone scissor mechanism as a function of applied load, corresponding to the data in Table 5.2. . 50
5.11 The scissor mechanism mounted in place on the walker legs. 52

Chapter 1

Introduction

Robotics has, over the past decades, progressively moved beyond the structured, predictable environments of the factory floor, where a robot's task, workspace, and interactions can largely be specified in advance, toward more open-ended settings: legged robots walking over uneven or unknown terrain, manipulators handling deformable or fragile objects, and machines operating in close physical proximity to people. This shift changes what is required of a robot's actuators. In a fully structured environment, precise, repeatable position control is usually sufficient, since the robot rarely needs to react to an unexpected force. In an unstructured or interactive environment, by contrast, a robot's actuators must routinely absorb disturbances, contacts, and loading conditions that were never explicitly planned for, and must do so safely, without the entire system needing to reason about every possible contingency in advance.

This is one of the central reasons why *compliance*, the ability of a mechanical system to yield, elastically or through control, in response to an external load, has become an important theme across many areas of robotics, including manipulation, human-robot interaction, and legged locomotion. Compliant systems are more forgiving of contact and more tolerant of modeling error, and, in the case of legged locomotion specifically, can be considerably more energy-efficient than fully rigid, actively-controlled alternatives, by allowing part of the dynamics of walking or running to emerge from the passive, elastic properties of the mechanism itself rather than from continuous active control effort. Robotic systems capable of compliant interaction with their environment are, for these reasons, an important and active area of research in modern robotics. Unlike rigid industrial manipulators, which are designed primarily for precise position control, many natural systems rely on compliance and distributed sensing to achieve stable and adaptive motion. Biological organisms often use small, low-effort corrective movements, generated by muscles and tendons whose mechanical properties are themselves compliant, to maintain balance and stabilize loads, rather than relying on a stiff structure driven by a fast, high-bandwidth control loop.

Within this broader landscape, this thesis explores the development of bio-inspired stabilization mechanisms for robotic systems. In particular, the project investigates how compliant actuation and sensing can be combined to achieve

adaptive stabilization behaviors similar to those observed in biological systems.

The work was carried out during a research internship at the ETIS laboratory (CY Cergy Paris Université) under the supervision of Prof. Alexandre Pitti. The internship is part of a broader research project investigating the integration and control of soft robotic actuation technologies, particularly HASEL [1] (Hydraulically Amplified Self-healing Electrostatic) actuators. These actuators represent a class of electro-hydraulic soft actuators capable of producing compliant motion with characteristics closer to biological muscle behavior than traditional rigid motors.

The long-term goal of the broader project is the design of a bio-inspired balancing joint capable of stabilizing heavy loads through small corrective motions. In this concept, soft actuators such as HASEL devices would act as fine adjustment mechanisms responsible for maintaining equilibrium, while larger actuators would generate the primary structural motion.

1.1 Motivation

Conventional position-controlled actuators, such as the smart servomotors used throughout early experimentation in this project, are well suited to precise trajectory tracking but poorly suited to physical interaction: their internal control loops actively resist external disturbances rather than yielding to them, and any compliant behavior must be synthesized through additional sensing and control layered on top of an otherwise stiff system. Biological systems achieve robust, adaptive stabilization very differently, through distributed, passively compliant structures, muscles and tendons, that respond to disturbance intrinsically, without requiring a fast sensing-and-control loop. This motivates exploring soft actuation technologies, such as HASEL actuators, that aim to reproduce this kind of intrinsic compliance in engineered systems, and it motivates asking what it practically takes to integrate such actuators into a real mechanical system.

1.2 Research questions

1. What mechanical and control constraints govern the practical integration of soft HASEL actuators into a quasi-passive walking mechanism originally designed for rigid electromechanical actuation?

2. What transmission architectures are best suited (or unsuited) to coupling a low-stroke, compliant actuator such as HASEL to a mechanical linkage subject to real, non-axial loading, such as that experienced by a walking leg?

3. For what class of applications, if not full-scale legged locomotion, is this type of HASEL actuator practically well suited?

1.3 Experimental robotic platforms

As an initial, preliminary phase of the internship, exploratory experiments were carried out on a small articulated robotic arm platform (the LeRobot SO-101 [11]), used to become familiar with compliant control strategies, sensor integration, and disturbance rejection using conventional, position-controlled hardware, ahead of a clear direction being set for the HASEL-related work. This exploratory phase is described in Chapter 3. While it does not feed directly into the mechanical design of the walker described later, it provided useful hands-on experience with IMU-based feedback and apparent-compliance control that shaped the author's general approach to the rest of the project.

The main body of the thesis concerns a quasi-passive bipedal walker, designed and built from scratch, inspired by minimally-actuated leg-extension walker geometries from the literature [13]. This platform serves as the testbed for evaluating the practical integration of HASEL soft actuators into a mechanical system, described in Chapters 4 and 5.

The insights obtained from the HASEL integration work inform the discussion, presented in Chapter 6, of the feasibility of this class of soft actuator for legged locomotion, and of the more general lessons, both mechanical and application-level, that emerged from the project.

1.4 Thesis structure

This thesis is organized as follows. Chapter 2 reviews relevant literature on compliant and soft robotics, HASEL actuators, and passive-dynamic walking. Chapter 3 presents preliminary, exploratory experiments carried out on the LeRobot SO-101 robotic arm, undertaken to build familiarity with compliant control before the walker/HASEL work began in earnest. Chapter 4 describes the mechanical design and characterization of the quasi-passive walker platform under conventional servo actuation. Chapter 5 presents the process of integrating HASEL actuators into the walker, including a dedicated actuator interface and the direct-drive, lever-based, and scissor-based transmission mechanisms that were designed, tested, and iterated upon. Chapter 6 discusses the combined findings, in particular the feasibility of HASEL actuation for this class of walker. Chapter 7 concludes the thesis and outlines directions for future work.

Chapter 2

Related Work

This chapter situates the work of this thesis within four bodies of prior research. Section 2.1 reviews compliance in robotics broadly, distinguishing passive from active (apparent) compliance, and introduces tensegrity structures as a further, structurally-embedded route to bio-inspired compliance pursued elsewhere in the host laboratory. Section 2.2 reviews HASEL soft actuators specifically, the actuation technology at the center of this thesis's main experimental contribution. Section 2.3 reviews passive-dynamic and quasi-passive walking, the class of legged locomotion platform used throughout Chapters 4 and 5. Finally, Section 2.4 discusses the position-versus-torque control limitation of low-cost smart servomotors, which explains why only *apparent* compliance, rather than genuine physical compliance, could be achieved on the preliminary SO-101 platform of Chapter 3. The chapter closes with a summary that ties these four threads together and identifies the specific gap this thesis addresses.

2.1 Compliance and Soft Robotics

Rigid, position-controlled actuators are poorly suited to physical interaction and disturbance rejection: any unexpected contact generates a large, abrupt force, since the actuator's internal controller resists deviation from its commanded position. Compliance, understood here as the ability to yield under load, addresses this in two broad ways. *Passive compliance* introduces an intentional elastic element into the actuator itself, most notably in the Series Elastic Actuator (SEA) proposed by Pratt and Williamson [17], which places a spring in series between the motor and the load; this provides shock tolerance, lower reflected inertia, and enables high-fidelity force control simply by measuring spring deflection, at the cost of reduced position bandwidth. *Active or apparent compliance*, by contrast, achieves compliant-*seeming* behavior purely through control, typically impedance or admittance control, without any dedicated elastic hardware element, by continuously adjusting the actuator's position or torque command in response to measured or estimated interaction forces.

The compliance strategies developed on the SO-101 arm in Chapter 3 fall squarely

into this second category: since the platform's servomotors expose no direct torque control and contain no physical elastic element, any compliant-seeming behavior can only be apparent compliance, produced by actively modulating the position reference. This distinction, between compliance that is a physical property of the actuator and compliance that is a computed behavior layered on top of a stiff actuator, is a recurring theme in this thesis, and it motivates the later interest in HASEL actuators (Section 2.2) as a route to actuators with some of the physical compliance properties of an SEA, but without a discrete mechanical spring.

A further, structurally different route to distributed compliance is offered by *tensegrity* structures, in which rigid compression elements are held in place entirely by a network of tensioned cables rather than by rigid joints, so that the structure as a whole, rather than any single localized actuator or spring, is what deforms and absorbs load. Tensegrity principles have long been used to model biological structures, most notably the vertebrate spine [8], on the basis that a cable-and-strut representation captures how biological tissue distributes mechanical load more faithfully than a conventional rigid-link, lever-based skeletal model. Within the host laboratory, this approach has been applied directly to postural balance robotics: Melnyk and Pitti [15] present a multi-segment tensegrity robot modeled on the vertebral column, controlled synergistically to maintain postural balance in a manner intended to mirror the distributed, structurally-embedded compliance of the biological spine. This line of work is complementary to the actuator-level approach to compliance pursued in this thesis: rather than seeking a single soft actuator to replace a rigid motor, the strategy explored here via HASEL, it distributes compliance throughout the mechanical structure itself. Both approaches share the same underlying motivation identified at the start of this section, moving away from rigid, actively-stiffened structures toward systems that are compliant by physical construction, and are worth considering together as complementary strategies toward the same broader goal of bio-inspired, adaptively compliant robotic structures.

2.2 HASEL Actuators

Hydraulically Amplified Self-healing Electrostatic (HASEL) actuators are a class of electrohydraulic soft actuators, first introduced by Acome et al. [1], that couple electrostatic and hydraulic forces to produce muscle-like contraction. In their basic form, a HASEL actuator consists of a flexible polymer shell partially filled with a dielectric liquid; a pair of external electrodes applies a high-voltage electrostatic force that displaces the liquid, deforming the shell and producing linear or rotary motion depending on the geometry. Because actuation occurs entirely through liquid displacement within a soft, deformable shell rather than through a rigid

mechanism, HASEL actuators are inherently compliant, and they are able to self-heal after local dielectric breakdown, a failure mode that would be catastrophic in a purely solid dielectric elastomer actuator. Taken together, these properties, muscle-like force-displacement behavior, intrinsic mechanical compliance, and robustness to local damage, position HASEL actuators as an attractive candidate for bio-inspired, muscle-like actuation in robotics, and they specifically motivate their investigation in this thesis as a soft-actuation alternative to the rigid servomotors used in the initial walker prototype (Chapter 4).

2.3 Passive-Dynamic and Quasi-Passive Walking

Passive-dynamic walkers exploit the natural, pendulum-like dynamics of a leg swinging under gravity to achieve efficient, human-like gaits with little or no active control. The concept was established by McGeer [14], who showed that a simple, unpowered two-legged mechanism, released on a shallow slope, could produce a stable, repeatable walking gait purely from its own mechanical dynamics and gravity, with no motors, sensors, or control system of any kind. This demonstrated that a substantial part of what makes a gait "walking-like" can be attributed to the passive mechanics of the leg and foot, rather than to active control, and it reframed legged locomotion as fundamentally a mechanical design problem as much as a control problem.

Quasi-passive walkers extend this principle by adding a small amount of actuation, typically periodic leg extension, on top of an otherwise passive mechanical structure, in order to inject the energy needed to sustain locomotion on level ground (compensating for losses at foot contact that a purely passive walker can only recover by walking downhill), while retaining much of the simplicity and efficiency of purely passive designs. A prominent example is the Cornell Ranger [4], a four-legged, knee-less quasi-passive biped that walked a 40.5-mile ultra-marathon on a single battery charge, demonstrating a Total Cost of Transport lower than that reported for any other legged robot at the time. Its efficiency stems from the same underlying principle: a lightweight, low-inertia leg design that lets passive pendulum dynamics do most of the mechanical work, with only a small, targeted amount of motor-driven actuation added where the passive dynamics alone cannot sustain the gait.

The walker platform developed in this thesis (Chapter 4) follows the minimally-actuated leg-extension geometry proposed by Islam et al. [13], who present a scalable quasi-passive bipedal walker using spherical-foot geometry and a single actuator per leg to produce stable 3D walking gaits from simplified, low-degree-of-freedom mechanics. This design was selected specifically because its geometric and actuation simplicity, a single linear leg-extension input per leg, with the walking gait emerging

largely from the passive foot and leg geometry, makes it a natural target for later replacement of the servo-based actuation with HASEL soft actuators, which are similarly limited to producing a single-axis, relatively small-stroke motion.

2.4 Position vs. Torque/Impedance Control in Servo Actuators

Low-cost "smart" servomotors, such as the Feetech STS3215 and FR0115M units used throughout this thesis, integrate their own microcontroller and run an internal position-control loop: the user commands a target joint angle, and the servo's internal PID controller generates whatever torque is needed to reach and hold that angle. This is convenient for rapid prototyping, since it removes the burden of closing a low-level control loop from the host computer, but it also means the actuator does not expose direct torque or current control to the user. Any external control strategy can therefore only act *indirectly* on the joint, by changing the commanded position and allowing the internal loop to do the rest. It cannot bypass the internal controller to command a force or an impedance directly, short of replacing the servo's firmware or driving the motor with custom electronics.

This is the fundamental hardware limitation behind every "apparent compliance" strategy explored on the SO-101 arm in Chapter 3: since torque cannot be commanded directly, and there is no physical elastic element in the drivetrain, compliant-seeming behavior can only be synthesized by continuously recomputing a position target from sensor feedback (orientation, motor load, or both) and letting the internal position loop track it. The resulting behavior can resemble a spring or a damper in its input-output characteristics, but it inherits the limitations of the underlying position loop, most notably gearbox backlash and closed-loop stiffness, and it remains fundamentally different from true impedance control implemented at the torque level, or from the physical compliance of a series elastic actuator (Section 2.2) or a HASEL actuator.

2.5 Summary

The threads reviewed in this chapter converge on the same underlying question addressed by this thesis: how much compliant, muscle-like behavior can be achieved on practical, low-cost robotic hardware, and what does it take to move from *apparent* compliance, synthesized through control on top of rigid, position-controlled actuators, toward actuators such as HASEL that are *physically* compliant by construction. Relatively little prior work directly connects these two threads for a hardware platform of the kind considered here. The compliance-control literature largely targets rigid actuators with more capable low-level interfaces, such as

torque-controlled or SEA-equipped manipulators, than the low-cost smart servos used in Chapter 3 [10, 17, 9], while the HASEL literature has largely focused on actuator-level development and characterization, with comparatively fewer works addressing system-level integration [1, 18]. This thesis sits at the intersection of these two threads: it first explores apparent compliance on accessible, position-controlled hardware (Chapter 3), then investigates, in practice, what is required to integrate a genuinely soft, physically compliant HASEL actuator into a complete legged mechanical system (Chapters 4 and 5).

Chapter 3

Preliminary Exploration: The SO-101 Robotic Arm

Before the direction of the project converged on the design and testing of a HASEL-actuated quasi-passive walker (Chapters 4 and 5), the early part of the internship was spent on exploratory, hands-on work with a small robotic arm platform, the LeRobot SO-101. This work was not intended as a core research track of the thesis, and its findings were not directly carried over into the mechanical design of the walker; rather, it served as a practical introduction to compliant control, IMU-based sensing, and the general limitations of position-controlled hardware, before a clearer research direction around soft actuation was established. It is included here as preliminary context for the reader, and because several of the general lessons it produced, particularly around the gap between actively-controlled "apparent" compliance and genuine passive compliance, remain relevant background for interpreting the HASEL work that follows.

3.1 Experimental Robotic Platform

To perform the initial experiments, a compact articulated robotic manipulator based on the LeRobot SO-101 platform was used. This robotic arm provides a simple and flexible hardware platform suitable for experimentation with motion control, sensor integration, and robotics algorithms. The arm consists of five revolute joints and a gripper mechanism, resulting in a total of six actuated degrees of freedom. The platform is compatible with the LeRobot software ecosystem, which provides tools for calibration, motion control, and kinematic modeling. Using this platform, it was possible to test different control strategies and sensing approaches without the need to design a complete robotic system from scratch.



Figure 3.1: The LeRobot SO-101 robotic arm platform used for the preliminary experiments [11].

3.2 Actuation System

The robotic arm is actuated by Feetech STS3215 [19] smart servomotors connected through an RS-485 communication bus, using a Feetech URT-1 USB-to-RS485 adapter for communication with the control computer. These smart servomotors integrate internal control electronics and position controllers, allowing joint positions to be commanded directly through serial communication. In addition to motion control, the motors provide telemetry data including joint position, motor velocity, estimated load, motor current, temperature, and supply voltage.



Figure 3.2: Feetech STS3215 smart servomotor used to actuate the SO-101 arm [19].

Although convenient for rapid prototyping, these motors present two limitations that are central to the compliance experiments described later in this chapter:

- The motors implement an internal position-control loop that cannot be fully bypassed by the user. External control algorithms attempting to modify joint behavior are therefore always mediated by, and can be counteracted by, this internal controller.
- Mechanical backlash is present in the transmission, producing small oscillations ("wiggle") around the commanded joint position, which reduces precision and complicates the implementation of compliant behaviors.

3.3 Software Framework

The robotic arm is controlled through a Python-based software framework built on the LeRobot ecosystem. The `lerobot-kinematics` [5] library provides the kinematic model of the robot and implements inverse kinematics algorithms, allowing Cartesian end-effector motions to be converted into joint commands. Using this framework it was possible to calibrate the robot joints, generate a calibration configuration file, control individual joint positions, execute trajectories, and move the end-effector in Cartesian space via inverse kinematics. The host-side control and kinematic scripts used for the compliance and stabilization experiments were implemented in Python 3.10, while IMU acquisition was handled separately by the Arduino. These experiments did not use ROS 2; a separate ROS 2 Humble demonstration, developed later as an independent exploratory activity, is described in Section 3.9.

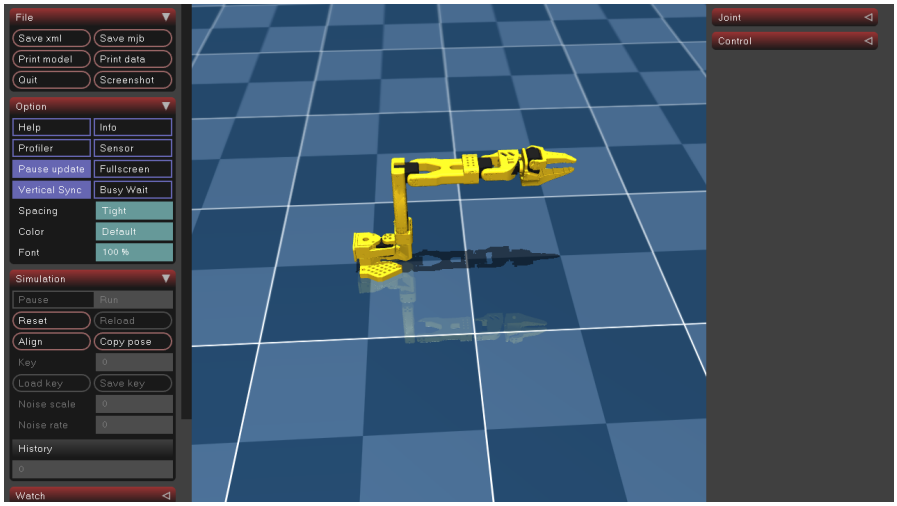


Figure 3.3: MuJoCo simulation environment used for kinematic modeling and visualization of the SO-101 arm.

3.4 Integration of an Inertial Measurement Unit

To measure the orientation of the robotic arm relative to gravity, an inertial measurement unit based on the MPU-6050 [12] sensor was integrated into the system. The IMU is connected to an Arduino Mega 2560 microcontroller [2], which reads accelerometer and gyroscope measurements and transmits them to the control computer via a serial interface. In the experimental setup, the IMU is mounted on the side of the gripper; since its mounting orientation was not mechanically constrained, a calibration procedure was implemented to estimate the orientation of the IMU relative to the robot coordinate frame.

By recording accelerometer measurements in several static arm poses, the gravity vector was observed from different sensor orientations, allowing a rotation matrix $R_{\text{imu}\to\text{robot}}$ to be estimated to transform IMU measurements into the robot reference frame. This calibration step allows the accelerometer to be used as a reliable sensor for measuring the orientation of the robot relative to gravity. The Arduino sketch used to acquire and stream the raw accelerometer and gyroscope readings over serial, from which this calibration was performed, is reported in Listing A.2 (Appendix A); a photo of the physical IMU and Arduino Mega setup, mounted on the SO-101 arm, is shown in Figure 3.5 below.

3.5 Preliminary Compliance Experiments

The primary objective of the initial experimental phase was to investigate how compliant behavior could be implemented using the available rigid, position-controlled hardware. Three approaches were explored.

Current-based compliance. External forces were estimated by monitoring motor current as a rough proxy for torque. This signal proved noisy and unreliable due to internal motor control and limited resolution.

Position-error based compliance. Commanded joint positions were modified based on the difference between measured and desired joint angles, allowing the arm to yield slightly under external force. Performance was limited by the internal servo control loop and mechanical backlash.

Glide-and-hold behavior. A hybrid strategy was implemented in which the robot follows external motion when pushed (glide) and gradually returns to a stable configuration afterward (hold). This produced partially compliant behavior but remained affected by servomotor hardware limitations.

These observations motivated the introduction of additional sensing, specifically orientation feedback from the IMU, to improve the robot's ability to detect and compensate for disturbances, leading to the postural stabilization experiment described next.

3.6 IMU-Based Postural Stabilization Experiment

3.6.1 Objective

The goal of this experiment was to investigate whether a simple posture stabilization mechanism could be implemented on a small rigid robotic arm using only orientation feedback and position-controlled servomotors, as an initial step toward bio-inspired stabilization mechanisms and compliant joints. The experiment focuses on stabilizing the pitch orientation of the end-effector by controlling a single joint (the elbow).

3.6.2 Control Architecture

The control architecture consists of two nested feedback loops. The outer loop, implemented in Python, uses the orientation measured by the IMU to modify the desired elbow position. This reference is then tracked by the servomotor's internal

position controller, which forms the inner feedback loop. Since direct torque control is not available, stabilization is therefore achieved indirectly through modulation of the joint position reference. The resulting cascade control architecture is shown in Figure 3.4.

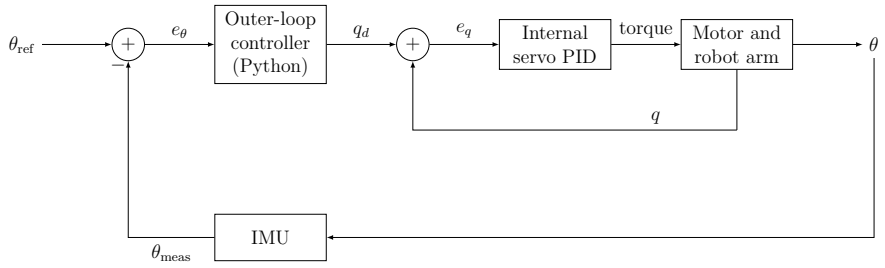


Figure 3.4: Cascade control architecture. The outer loop uses IMU orientation feedback to modify the desired joint position, while the inner position-control loop is implemented by the servomotor's internal PID controller.

3.6.3 IMU-Based Orientation Estimation

The MPU-6050 provides raw three-axis accelerometer measurements a_x, a_y, and a_z. These values are first scaled and grouped into the acceleration vector

$$\mathbf{g}_{\text{imu}} = \frac{1}{16384} \begin{bmatrix} a_x \\ a_y \\ a_z \end{bmatrix}.$$

Here, $\mathbf{g}_{\text{imu}}$ is a 3×1 vector representing the measured acceleration in the IMU reference frame, expressed in units of gravitational acceleration (g).

To reduce measurement noise, a first-order low-pass filter is applied:

$$\mathbf{g}_{f,k} = (1 - \alpha)\mathbf{g}_{f,k-1} + \alpha \mathbf{g}_{\text{imu},k}.$$

Here, $\mathbf{g}_{f,k}$ is the 3×1 filtered acceleration vector at the current sample, $\mathbf{g}_{f,k-1}$ is the filtered vector from the previous sample, and α is a scalar filter coefficient. In the implemented system, $\alpha = 0.18$.

The filtered acceleration vector is then transformed into the robot coordinate frame:

$$\mathbf{g}_{\text{robot}} = \mathbf{R}_{\text{imu}\to\text{robot}} \mathbf{g}_f.$$

Here, $\mathbf{g}_{\text{robot}}$ is a 3×1 vector and $\mathbf{R}_{\text{imu}\to\text{robot}}$ is a 3×3 coordinate-frame transformation matrix.

Under static or slow-motion conditions, the accelerometer mainly measures the direction of gravity. Therefore, roll ϕ and pitch θ can be estimated from the components of the robot-frame acceleration vector

$$\mathbf{g}_{\text{robot}} = \begin{bmatrix} g_x \\ g_y \\ g_z \end{bmatrix}.$$

The two orientation angles are calculated as

$$\phi = \text{atan2}(g_y, -g_z),$$

and

$$\theta = \text{atan2}\left(g_x, \sqrt{g_y^2 + g_z^2}\right).$$

Both ϕ and θ are scalar quantities and are converted to degrees in the software implementation.

3.6.4 Interpretation as Apparent Stiffness

Although the system contains no physical elastic element, the proportional feedback produces behavior similar to a virtual restoring stiffness: as the arm deviates from its reference orientation, the IMU detects a pitch error, the controller modifies the elbow position target, and the servo's internal PID generates torque to reach the new position, with corrective motion magnitude increasing with orientation error. Unlike a physical spring, however, this restoring behavior is *active* (dependent on sensing and computation), *delayed* (due to discrete-time measurement and command intervals), and *limited by actuator dynamics* (gearbox backlash, internal controller behavior). The system therefore produces *apparent stiffness*, not true passive mechanical stiffness.

3.6.5 Software Architecture Considerations

Initial implementations revealed significant delays caused by serial buffering and blocking actuator commands. The software architecture was therefore modified to separate sensing and control into independent tasks: a dedicated IMU acquisition thread continuously reads and parses sensor data, while the control loop runs independently and always uses the most recent available sample, ensuring the controller operates on fresh data rather than a delayed serial buffer.

3.6.6 Observed Limitations

Several hardware limitations influenced the observed behavior:

- **Servo backlash and compliance:** gear reductions in the STS3215 servos introduce noticeable backlash, so small commanded position changes may not immediately translate into external motion.
- **Internal servo controller:** the internal PID attempts to maintain the commanded position with high stiffness, which can interact with the outer loop and produce oscillatory "wiggling" behavior.
- **Limited torque sensing:** the servos do not provide accurate torque feedback, so the controller cannot directly regulate force or stiffness.
- **Communication latency:** serial communication introduces additional delay between sensing and actuation.

3.7 IMU + Effort-Based Elbow Compliance

To achieve apparent compliant behavior using both global orientation feedback and local interaction sensing, a second controller was developed combining the IMU-based pitch term with an effort-based term derived from motor load. Only the elbow joint (joint index 3) was controlled, with all other joints held at a nominal configuration, in order to isolate the behavior of the control law and validate the sensing and control strategy before considering multi-joint coordination.

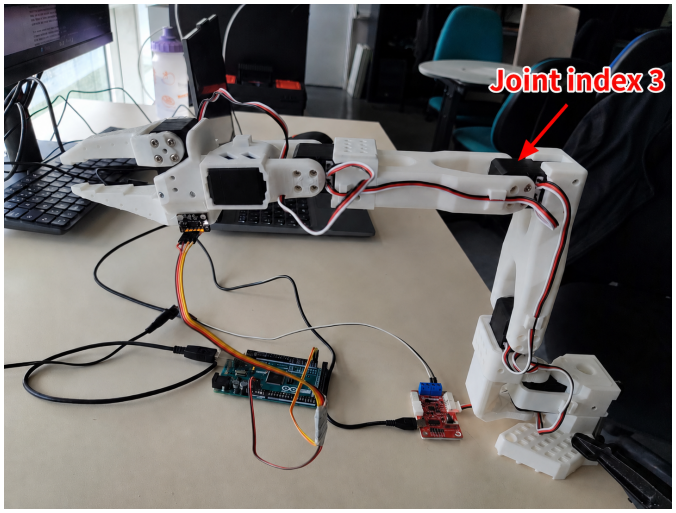


Figure 3.5: Experimental setup for the IMU-based postural stabilization and effort-based compliance experiments: the SO-101 arm with the MPU-6050 IMU and Arduino Mega interface visible on the desk.

The control law consists of two additive terms. The IMU-based term maps the pitch error relative to a reference pose into an elbow position offset:

$$\Delta q_{\text{IMU}} = K_{\text{pitch}}\, e_{\text{pitch}}.$$

This term produces a smooth and continuous correction when the structure tilts. The effort-based term uses the motor's measured load, after subtracting a bias, to detect external interaction. When the effort magnitude exceeds a predefined threshold, the corresponding offset is

$$\Delta q_{\text{effort}} = K_{\text{effort}}\ \text{sign}(e_{\text{effort}})\,(|e_{\text{effort}}| - e_{\text{th}})\,.$$

This allows the controller to detect and respond to externally applied pushes even when the variation measured by the IMU is small. The final elbow target is obtained by adding the two corrections to the initial joint position:

$$q_{\text{elbow,target}} = q_{\text{start}} + \Delta q_{\text{IMU}} + \Delta q_{\text{effort}}.$$

The resulting target is rate-limited to ensure smooth motion and avoid abrupt changes in the commanded joint position.

The resulting behavior showed smooth compliance when moving upward (aided by mechanical backlash allowing IMU variation), improved compliance when pushing downward due to the effort-based term, no strong return to the initial pose, and stable motion without excessive oscillation after tuning. This demonstrates that IMU feedback alone is insufficient for symmetric compliance, and that effort

feedback is necessary to detect interaction in directions where the structure is otherwise stiff; combining both signals produced a more balanced response. This controller does not implement true impedance or torque control, but creates *apparent compliance through position modulation* driven by inertial and effort feedback, representing a good level of compliance achievable given the hardware constraints. The corresponding control loop implementation is reported in Listing A.3 (Appendix A).

3.8 Intermediate Inverted-Pendulum Setup

To transition the focus from local, single-joint compliance toward global stabilization dynamics, more directly aligned with the long-term bio-inspired balancing objective, a preliminary balancing experiment was defined using the pose $[0.0,\ -0.25,\ -1.2,\ 0.0,\ 0.0,\ 0.0]$. In this configuration, the distal portion of the arm acts as an unstable body, while the proximal shoulder-lift joint (joint index 2) serves as the corrective actuator, with the end-effector IMU providing the global tilt signal. This reduces the balancing task to a simplified single-input stabilization problem.

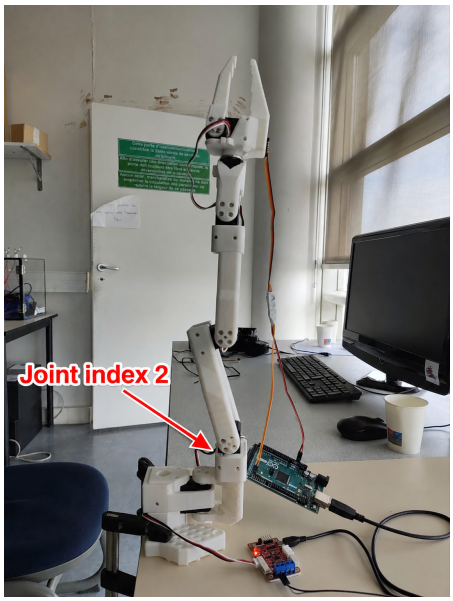


Figure 3.6: SO-101 arm in the preliminary inverted-pendulum-like pose used for the balancing experiment.

Although the structure is not a classical single-link inverted pendulum, it can be approximated as a proximal actuated joint stabilizing a distal multi-link body,

sufficient for a first experimental validation of inertial-feedback balancing. A direct cart-pole analogy is not exact for this platform, since corrective motion is generated by a rotating joint rather than a translating base; a single-plane pendulum on an actuated pivot, focusing on near-upright stabilization under small perturbations, was identified as a more appropriate simplified intermediate model for future work.

3.9 Additional Exploration: ROS 2-Based Behavior Control

As a further, separate piece of preliminary exploration on the same SO-101 platform, a small standalone demonstration was also developed using ROS 2 Humble Hawksbill [16], again with the explicit goal of building general familiarity with robot software architectures and real-time control before the project's direction had converged on the walker and HASEL actuation. This demonstration is unrelated to the compliance experiments described above and did not reuse their hardware or controller: it was built as an independent ROS 2 package set (`so101_hardware_py`, `so101_control_py`, `so101_description`, `so101_bringup`), interfacing the SO-101 arm and an MPU6050 IMU (again mounted near the end-effector) with a behavior-selection controller, and visualized through an RViz digital twin of the robot.[1]

The system implemented a simple sensing-to-behavior pipeline: the IMU-based push detection identified both the occurrence and direction (left/right) of an external disturbance applied to the arm, and this triggered one of several pre-programmed expressive joint-trajectory behaviors, for example, a recoil-and-slow-recovery motion or a more aggressive corrective motion, selected and switched live via ROS 2 parameters. Beyond exercising the ROS 2 control and visualization stack, this demonstration did not feed into, and was not intended to feed into, the mechanical or control design of the walker platform; it is mentioned here only for completeness, as a further example of the exploratory groundwork carried out on the SO-101 arm during the early part of the internship, using different actuators and a different control architecture from those used in the rest of this preliminary chapter.

[1] Source code available at: `https://github.com/bighianifrancesco-gif/so101-ros2-behaviors`

3.10 Summary

This chapter documented a preliminary, exploratory phase of the internship, carried out on the SO-101 arm before the project's direction converged on HASEL integration into the quasi-passive walker. The compliance experiments demonstrated that postural stabilization and interaction-aware compliance can be approximated on rigid, position-controlled hardware through active control, but only as an *apparent* form of compliance, layered on top of, and ultimately limited by, the servo's internal PID loop, backlash, and lack of torque sensing; a separate, unrelated ROS 2-based behavior-control demonstration further contributed to general familiarity with robot software architectures. This distinction between apparent, actively-computed compliance and genuine physical compliance is the main conceptual takeaway carried forward from this exploratory phase; neither it, nor the ROS 2 demonstration otherwise shaped the mechanical design of the walker platform described in Chapters 4 and 5, which was developed as a separate, largely independent line of work once the HASEL-focused direction of the internship was set.

Chapter 4

Experimental Platform: A Quasi-Passive Walker

4.1 Design Rationale

Motivated by the long-term goal of soft-actuated, bio-inspired locomotion, the objective of this phase of the project was to establish a working mechanical architecture for a quasi-passive bipedal walker, inspired by the geometries and principles described by Islam et al. [13] on minimally-actuated leg-extension walkers (see Chapter 2). The goal was not to reach a final, optimized design, but to establish a platform that could later be extended for the integration of HASEL actuators, described in Chapter 5.

The system was modeled entirely from scratch using the Onshape CAD platform, without relying on existing ready-made designs. The design process focused on preserving the key geometric relationships described in [13], while adapting dimensions and component layout to the available hardware and to a larger overall scale, in order to accommodate the intended actuators and leave sufficient space for future HASEL integration.

4.2 Mechanical Architecture

The prototype is based on a quasi-passive architecture comprising:

- a passive hip joint realized through a fixed axle;
- two legs connected to the axle and free to rotate;
- a telescopic lower leg section designed to allow controlled extension;
- actuation implemented using conventional servomotors approximating the leg-extension mechanism;
- curved feet designed as portions of a spherical surface.

The nominal leg length was set to approximately 280–290 mm, with a total height (fully extended) of about 350 mm. Particular attention was given to the design of the feet, a critical element for passive and quasi-passive walking: rather than approximating the shape using planar curves, the foot was generated as a spherical cut, ensuring consistent curvature in both sagittal and frontal planes, with a radius of curvature in the range of 260–290 mm. The center of curvature of the foot was positioned with a forward and downward offset relative to the hip joint, reproducing the non-concentric configuration described in the reference geometry, and a lateral offset ("y_{gap}") of approximately 18 mm was introduced between the two feet to promote lateral stability and avoid purely symmetric rocking.

The upper leg was designed as a structural bracket including a cylindrical hub for the passive hip joint, a guide structure for the telescopic lower leg, and a mounting interface for the servomotor. Due to the specific geometry of the available servomotors (Feetech FR0115M, without standard mounting ears), a custom mounting solution was implemented using a constrained pocket and clamping strategy, ensuring both rigidity and removability. The FR0115M is a digital, dual-shaft, metal-gear servo with a peak stall torque of approximately 15 kg·cm at 6 V and standard PWM control (pulse width 500–2500 µs) [7], providing ample torque margin for the leg-extension loads involved.

The two lateral leg assemblies are separated by a set of 3D-printed PLA spacers mounted internally, between each leg and the central hub that also carries the Arduino Mega controller; these are the spacers referred to elsewhere in this thesis by length (e.g. the 20 mm spacer used in the best-performing configuration, Section 4.6), and swapping them for a shorter or longer version changes the lateral distance between the legs, and hence the robot's overall width, without redesigning the leg brackets. A second, separate pair of PLA spacers is fitted externally on the hip axle, just outboard of each leg; these are simple press-fit retainers rather than width-setting parts, and their only function is to prevent the legs from sliding axially off the ends of the hip rod. Neither type of spacer is mechanically fastened: both rely purely on press-fit friction against the axle. The passive hip joint itself uses no dedicated rolling-element bearing: rotation is provided directly by PLA sliding against the steel rod passing through the hub, with a small amount of clearance deliberately left in the fit to keep friction low and allow the legs to rotate freely under gravity, consistent with the quasi-passive operating principle of the walker.

The actuation system is based on standard servomotors controlled by an Arduino Mega, using open-loop periodic motion to approximate the leg-extension profile described in the reference paper. The telescopic leg was designed to allow approximately 30 mm of stroke, corresponding to about 10% of the nominal leg length, consistent with quasi-passive operation.

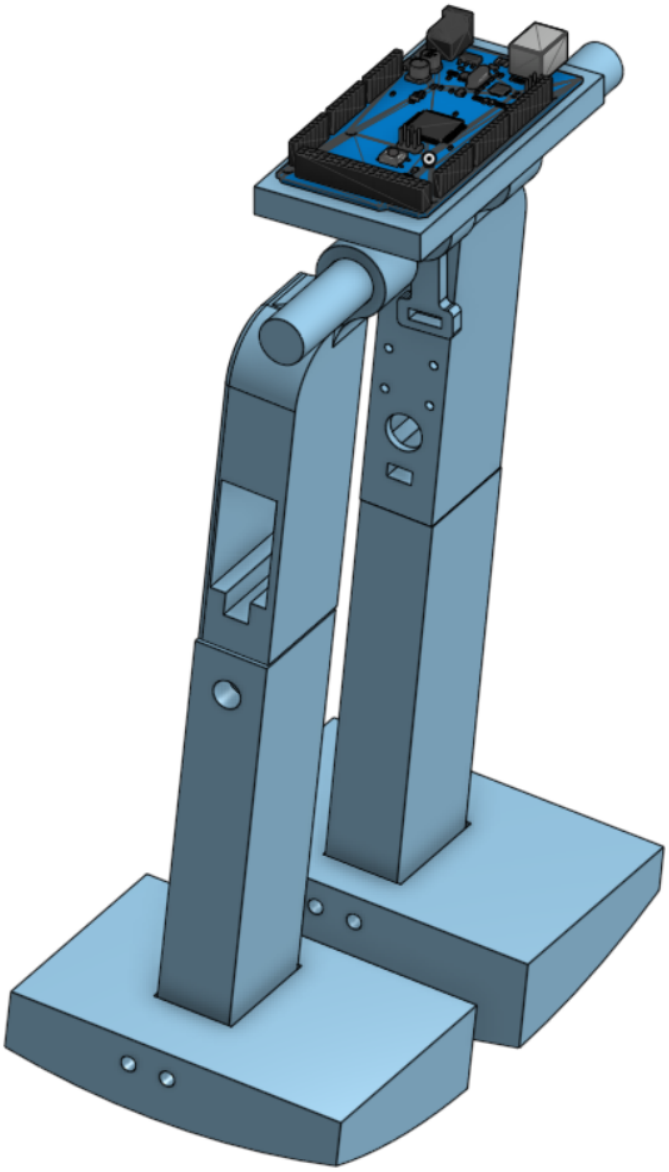


Figure 4.1: Early CAD assembly of the quasi-passive walker.



Figure 4.2: The early walker prototype, actuated by the original crank–connecting rod mechanism described below, with the Arduino Mega controller visible on top.

4.3 Electronics and Power Distribution

The two leg servomotors and the Arduino Mega controller were both powered from a single 5 V source: an Xmove-brand USB power bank (cream-colored housing with a speckled, granite-like finish, two USB-A output ports, and a gray silicone carry strap), weighing 205 g. This battery is one of the two largest contributors to the walker's total mass (Section 4.6) and, being significantly heavier and more compact than the small cell assumed in the reference design [13], was directly responsible for the excessive forward-pitching tendency discussed below.

The Arduino Mega was mounted on a custom prototyping shield, from which the 5 V and ground rails were distributed directly to both servomotors in parallel with the Arduino's own supply, rather than being routed through the microcontroller's regulated output. A single dedicated wire carried the PWM signal from each Arduino digital output to the corresponding servo signal line, while the servos' power

connections were wired independently to the shared 5 V rail. The complete power-distribution and signal-routing architecture is shown schematically in Figure 4.3.

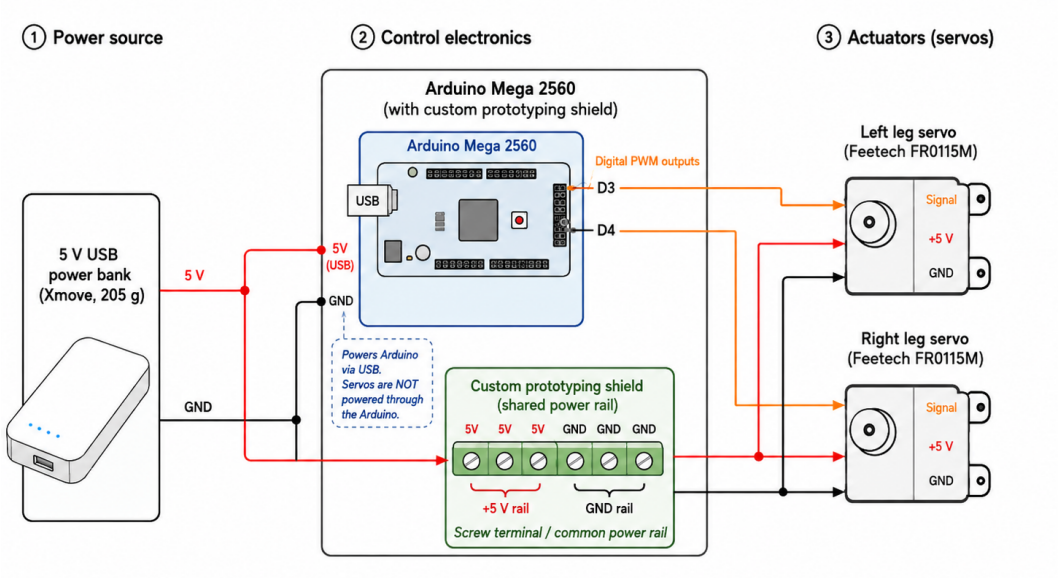


Figure 4.3: Schematic of the electrical connections between the 5 V USB power bank, Arduino Mega with custom prototyping shield, and the two Feetech FR0115M leg servomotors. Servo power is distributed directly from the shared 5 V rail, while the two PWM control signals are routed independently from the Arduino.

This separation of the low-current signal path from the higher-current power path avoided loading the Arduino's own supply regulation with the servos' current draw, while requiring the Arduino and the servomotors to share a common ground and battery voltage. The physical implementation of this power-distribution system is shown in Figure 4.4.

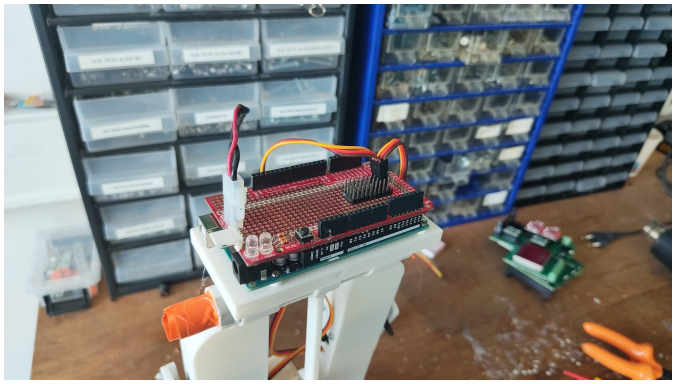


Figure 4.4: Arduino Mega mounted on the custom prototyping shield used to distribute power to the walker's servomotors. The shield's JST connector (left, with red/black leads) connects to the 5 V USB power bank; PWM signal wires run separately to the servo headers, while power is distributed directly to the servos rather than through the Arduino's own regulator.

4.3.1 Simplicity of the Gait-Generation Code

A notable practical feature of this open-loop actuation scheme, beyond its mechanical robustness (Section 4.7), is the simplicity of the software required to implement it. The complete gait-generation sketch (Listing A.1, Appendix A) consists of two `Servo` objects driven by a pair of sine functions, phase-shifted by 180°, with the oscillation frequency, amplitude, and per-leg neutral angle exposed as a handful of tunable constants. The entire control loop is sensing-free, with no matrix operations, filtering, or state estimation of any kind, and amounts to fewer than 40 lines of standard Arduino C++. Beyond ease of implementation and tuning, this has a direct practical benefit for miniaturization: because the controller requires only enough computing power to evaluate two `sin()` calls and write two PWM outputs at a modest update rate (50 Hz in our implementation), the same gait-generation approach is not tied to a relatively capable board such as the Arduino Mega used here, and could in principle run on far more constrained microcontrollers, including the low-pin-count, kilobyte-scale-memory parts typically used in microrobotics, without modification to the underlying control strategy. This is a direct software-level consequence of the mechanical design philosophy discussed throughout this chapter: by pushing as much of the walking behavior as possible into the passive mechanics of the leg and foot, the corresponding control problem is reduced to generating two simple periodic signals, rather than requiring the real-time state estimation and feedback computation that closed-loop legged controllers typically demand.

4.4 Crank–Connecting Rod Mechanism for Leg Extension

The actuation mechanism initially tested for the telescopic leg extension proved excessively flexible and mechanically unstable, due to insufficient structural rigidity and poor guidance of the moving elements, resulting in wobbling, inconsistent motion transmission, and unreliable leg extension during dynamic tests. A mechanically sturdier crank–connecting rod design was therefore developed, converting the rotational motion of the servomotor into an approximately linear displacement of the telescopic lower leg. The mechanism consists of a crank radius $r = 25.5$ mm, a connecting rod length $l = 60$ mm, and a telescopic slider constrained to move along a single axis.



Figure 4.5: Close-up of the crank joint at the leg's actuation point, showing the servo mounting bracket and the crank arm connecting to the servo horn.

The kinematic geometry of the mechanism is shown in Figure 4.6. The crank angle θ is defined with respect to the vertical axis, while the slider displacement $x(\theta)$ is measured along the horizontal direction.

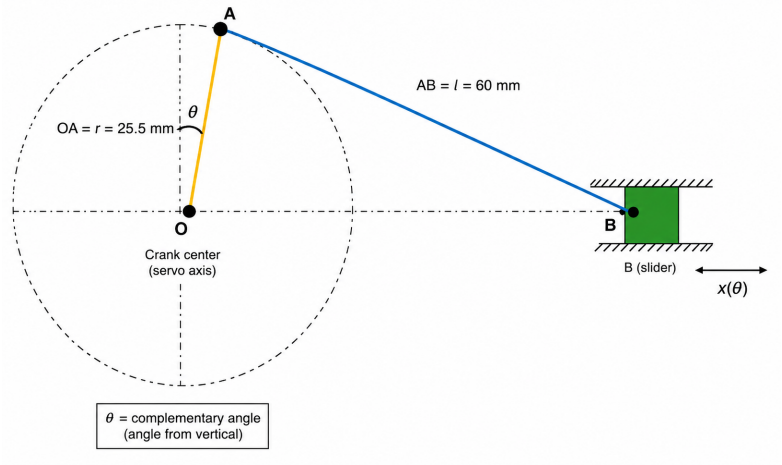


Figure 4.6: Kinematic diagram of the crank–connecting rod mechanism, with crank radius $r = 25.5$ mm, connecting rod length $l = 60$ mm, and crank angle θ measured from the vertical axis.

For an ideal in-line crank–slider mechanism, the slider position follows directly from the geometric closure imposed by the fixed connecting-rod length. With the angle convention adopted in Figure 4.6, the coordinates of point A are $r \sin\theta$ in the horizontal direction and $r \cos\theta$ in the vertical direction. The connecting rod therefore satisfies

$$(x - r\sin\theta)^2 + (r\cos\theta)^2 = l^2.$$

Solving for the slider position gives

$$x(\theta) = r\sin\theta + \sqrt{l^2 - r^2\cos^2\theta}.$$

This is the standard crank–slider kinematic relationship, expressed according to the angle convention used here. When the connecting rod is longer than the crank, the contribution of the square-root term varies less than the crank-dependent term, and the variable component of the slider motion can be approximated as

$$\Delta x \approx r\sin\theta.$$

The resulting motion is therefore approximately sinusoidal, while still retaining the geometric nonlinearities characteristic of crank–slider systems. The theoretical peak-to-peak displacement over a full crank excursion is approximately $2r = 51$ mm, although the effective usable stroke is smaller in practice due to mechanical limits, servo angle restrictions, and stability considerations. This revised mechanism significantly improved the rigidity of the telescopic actuation system and reduced unwanted lateral oscillations observed in the previous prototype version.

4.5 Mechanical Redesign and Dynamic Stability Adjustments

During the first dynamic walking tests, the robot exhibited an excessive forward pitching tendency, attributed to the center of mass being positioned too far forward relative to the intended passive-dynamics configuration. This was primarily because the battery used in the prototype is significantly heavier than the compact power source assumed in the reference design, resulting in a larger forward moment. To compensate, the hip rotation axis was repositioned from 17 mm to 13 mm from the vertical central plane (an offset of approximately 4 mm), reducing the effective forward offset between the body mass and the foot curvature center, and the spherical feet were reprinted with the new center of rotation to preserve geometric consistency.



Figure 4.7: The two printed upper leg brackets side by side, before (17 mm) and after (13 mm) the hip-axis offset adjustment.

Since the final mass distribution depends on several non-final components (battery, servomotors, wiring, and future HASEL integration), the hip-axis offset was tuned experimentally rather than fixed solely from the CAD model. This is consistent with the general sensitivity of passive and quasi-passive walkers to

center-of-mass position, foot geometry, friction, joint play, and actuation timing: an empirical tuning phase in this context is a necessary part of the design process rather than a shortcoming of the CAD-based design. Offsets of 6 mm and 3 mm (relative to the original configuration) were tested to identify the best compromise between passive forward lean and dynamic stability.

4.6 Experimental Tuning Phase

Following the iterative mechanical redesign, a sufficiently robust testing prototype was obtained, allowing the transition from mechanical debugging to a systematic experimental characterization of the gait generation parameters. The complete servo-driven walker, in its final tested configuration, was measured at a total mass of 862 g, of which the 205 g battery (Section 4.3) is the single heaviest component. This is consistent with its identification as the main driver of the forward-pitching behavior discussed above. A parametric exploration was carried out, testing combinations of actuation frequency (Hz) and extension amplitude (mm), with the goal of constructing a performance map highlighting the operating regions that produce stable forward locomotion.

4.6.1 Amplitude–Frequency Characterization

For each tested parameter pair, the resulting gait was assigned a qualitative performance score from 1 to 4 (1: no walking, 2: unstable walking, 3: acceptable walking, 4: stable walking). Two configurations were compared: without padded soles and with padded soles added to the feet.

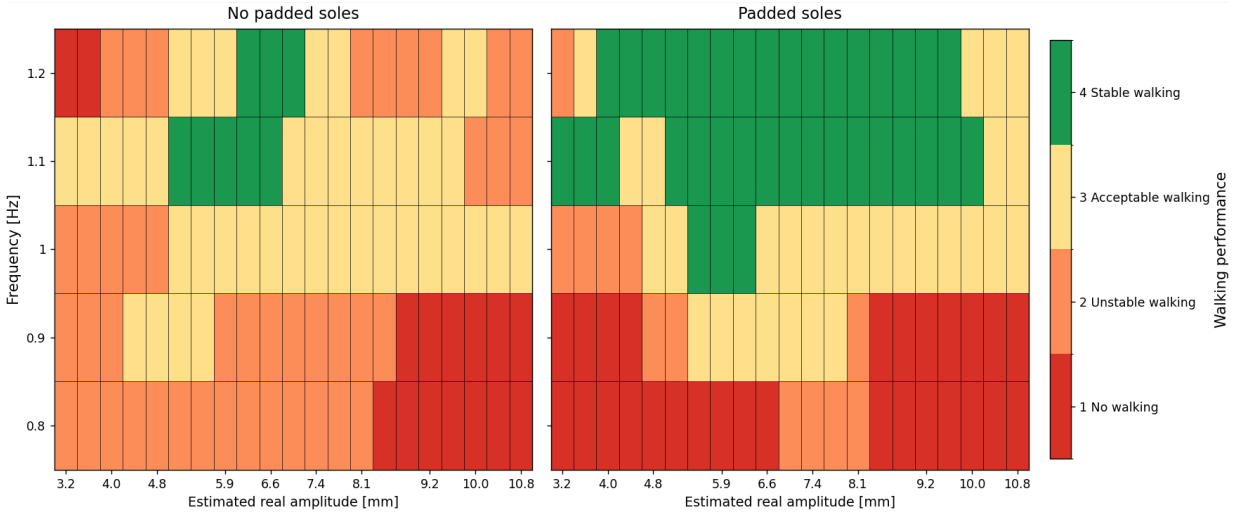


Figure 4.8: Walking performance as a function of actuation frequency and estimated real amplitude, without padded soles (left) and with padded soles (right). Color indicates qualitative walking score, ranging from 1 (no walking) to 4 (stable walking).

The comparison shows a clear improvement in walking performance when padding is added to the feet. Without padded soles, stable walking is limited to a narrow region of the tested parameter space, mainly around intermediate amplitudes and higher frequencies; at lower frequencies and larger amplitudes, the gait becomes unstable or fails. With padded soles, the region of stable walking becomes wider and more continuous, particularly between approximately 5 and 10 mm of amplitude and across the upper part of the tested frequency range. This suggests that the padded soles improve foot-ground interaction, likely by increasing friction and reducing slipping during stance, making the robot less sensitive to small changes in actuation parameters and able to maintain a more robust gait over a broader operating region. Foot-ground contact therefore plays a major role in the stability of the prototype, with padding expanding the range of amplitude–frequency combinations producing acceptable or stable walking, rather than simply improving a single operating point.

4.6.2 Best Configuration

As a brief reminder before discussing the results below: the "spacer" referred to throughout this section is the internal 3D-printed PLA spacer described in Section 4.2, mounted between each leg and the central hub to set their lateral distance apart (distinct from the separate, non-adjustable press-fit spacers on the outside of the hip axle, whose only role is to keep the legs from sliding off axially);

different spacer lengths can be swapped in without redesigning the leg brackets, which is what made it practical to sweep this parameter experimentally.

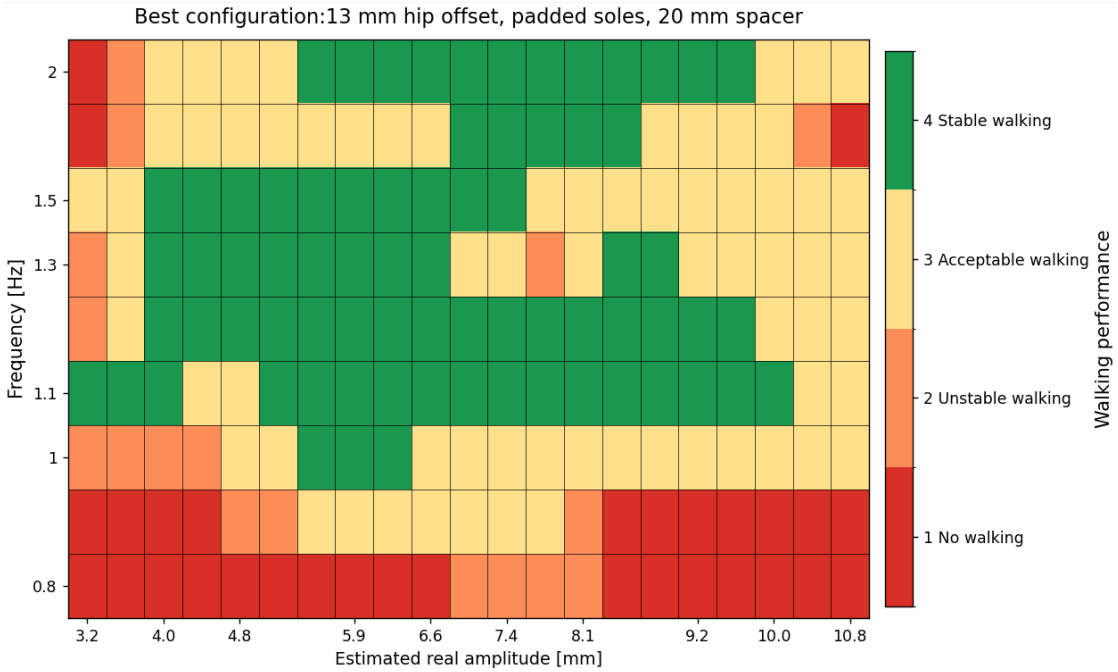
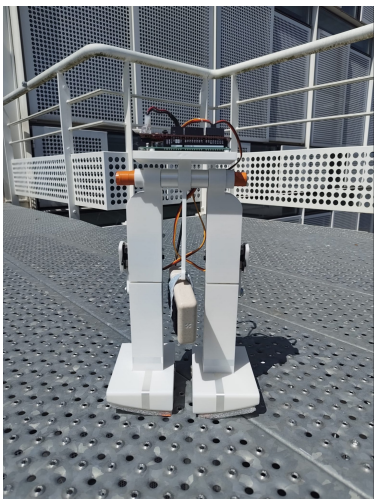


Figure 4.9: Walking performance map for the best-performing configuration: 13 mm hip offset, padded soles, 20 mm spacer.



Figure 4.10: The finished, servo-driven walker in its best-performing configuration (13 mm hip offset, padded soles, 20 mm spacer), the configuration used throughout the frequency–amplitude and velocity characterization presented in this chapter.



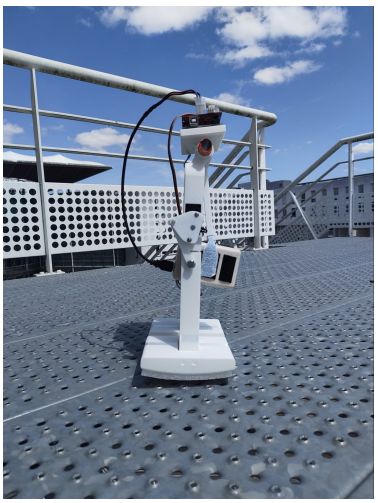


Figure 4.11: The finished walker during outdoor testing, viewed from the front (left) and from the side (right).

The best-performing configuration was obtained with a 13 mm hip offset, padded soles, and a 20 mm spacer. This result can be interpreted mechanically: the 20 mm spacer provides a favorable compromise in lateral width, narrower than a 30 mm spacer (which restricts side-to-side oscillation needed for walking) but wider than a 10 mm spacer (which leads to excessive oscillation and reduced gait robustness). The 13 mm hip offset similarly provides an effective balance for forward walking: shifting the hip axis gives the robot a slight forward lean sufficient to promote forward progression, without pitching so far forward as to cause instability, premature falling, or gait stalling.

4.6.3 Velocity Testing

To further evaluate the best mechanical configuration, additional trials measured the time required for the walker to cover a fixed distance of 2 m, at two selected actuation amplitudes while varying actuation frequency.

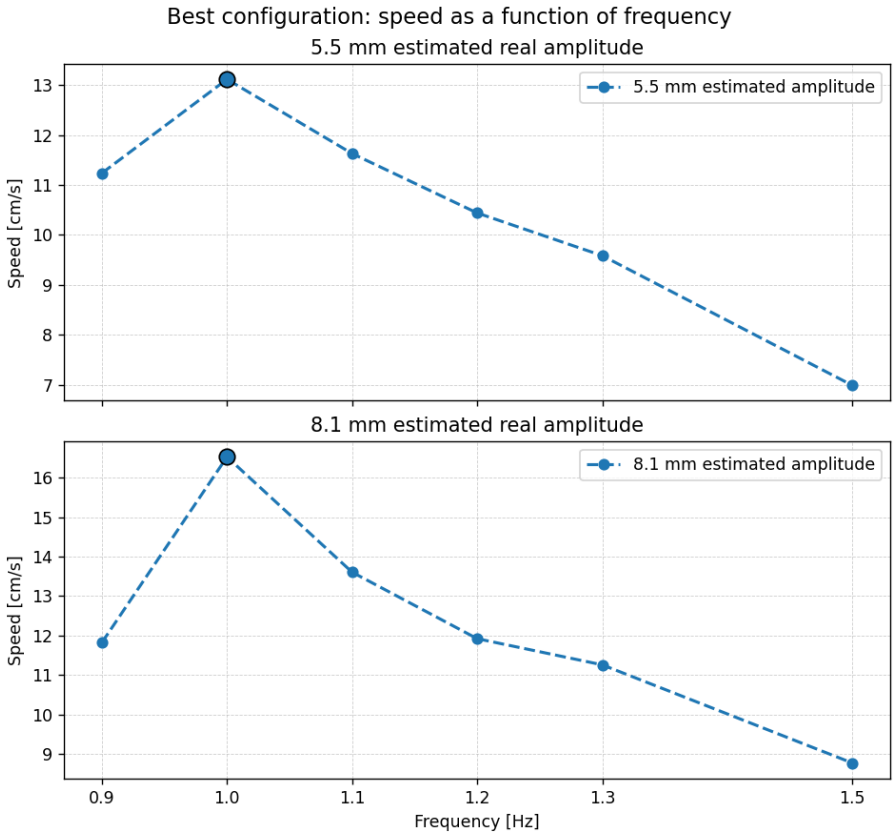


Figure 4.12: Walking speed as a function of actuation frequency, for the best configuration (13 mm hip offset, padded soles, 20 mm spacer), at two estimated real amplitudes.

For each frequency–amplitude operating point, only one or two 2 m runs were performed. The resulting speed measurements should therefore be interpreted as an exploratory characterization of the frequency trend rather than as statistically robust estimates of mean walking speed; no confidence intervals or error bars are reported.

For both tested amplitudes, the highest walking speed was obtained at approximately 1.0 Hz, with the larger amplitude of about 8.1 mm producing the highest measured speed. Below this frequency the gait is less effective, while above 1.0 Hz speed progressively decreases despite the robot remaining able to walk in several cases. This suggests that, among the tested values, approximately 1.0 Hz is the best-performing operating frequency and may lie close to the natural mechanical oscillation of the walker, allowing efficient forward progression; increasing frequency beyond this tested point cycles the legs faster without a corresponding increase in forward velocity, as the gait becomes less efficient. The best tested combination for speed was therefore the 13 mm hip offset, padded soles, 20 mm spacer configuration, with an estimated real amplitude of about 8.1 mm and an actuation frequency of 1.0 Hz.

4.7 IMU-Based Feedback Attempts and Mechanical Optimization Priority

A first attempt was made to introduce closed-loop feedback using the MPU6050 IMU, using measured body inclination and angular velocity to dynamically adjust the actuation amplitude of the telescopic legs in real time, aiming to compensate for asymmetries and improve walking stability. In practice, the IMU readings proved too noisy to reliably connect to the walker's actual physical posture during walking: the measured orientation did not track the robot's real gait cycle in a clean or consistent way, making it difficult to trust the signal enough to base a correction on it. This sensing-side problem was compounded by the walker's control sensitivity: because the locomotion mechanism operates close to a passive-dynamics regime, even a correction computed from a trustworthy signal would need to be small, and with a noisy signal, minor amplitude modifications computed from it could significantly alter the gait, often producing effects larger than the intended correction. Achieving reliable closed-loop stabilization through IMU feedback was therefore found to be considerably more challenging than initially anticipated, and further development of the feedback controller was postponed in favor of continued mechanical optimization, which was judged to offer greater benefit at this stage of the project than increasingly complex control strategies. The IMU was ultimately not carried forward into the final walker design: the sensor data did not provide a sufficiently clean or reliable indication of gait quality to justify the added control

complexity, and the simplest viable actuation scheme, two independent, phase-shifted sinusoidal position commands, one per leg, with no sensor feedback, was retained instead, consistent with the design philosophy of prioritizing mechanical robustness over control sophistication at this stage of the project.

One important observation made during this phase concerned ground-contact compliance. While running early walking trials on the bare, rigid lab floor, the gait looked inconsistent and difficult to reproduce from one trial to the next, with the feet appearing to slip at the moment of contact rather than gripping cleanly. This suggested a hypothesis: that the walker's stability was being limited not just by the actuation parameters, but by insufficient friction and cushioning at the foot–ground interface, and that adding some compliance there might absorb impact and reduce slipping enough to make the gait more repeatable. To test this, a simple foam layer was added to the underside of each foot as an experimental pad, ahead of any more permanent implementation, and the walker was re-run under otherwise identical conditions. The improvement was immediately noticeable by eye, and the systematic amplitude–frequency comparison presented earlier in this chapter (Section 4.6, Figure 4.8) subsequently confirmed this initial impression with data: padded soles widened the stable-walking region substantially rather than only helping in isolated cases, supporting the original hypothesis that foot-ground compliance, not just actuation tuning, was a limiting factor.

The lateral spacing between the two legs was tuned following a similar hypothesis-driven process. Since the walker's forward progression depends on side-to-side weight transfer between the legs, it seemed reasonable to expect that this spacing would trade off lateral mobility against stability, and the same amplitude–frequency testing procedure used for the padding comparison was repeated at a small number of different spacer widths to check this directly, rather than trusting the reference design's geometric scaling alone. The results (Section 4.6) confirmed the expected trade-off and identified 20 mm as the best-performing width among those tested.

4.8 Summary

By this stage, the walker had converged toward a mechanically stable, characterized architecture (13 mm hip offset, padded soles, 20 mm spacer, crank–connecting rod leg actuation), validated through systematic amplitude–frequency and velocity testing under conventional servo actuation. This electromechanical baseline serves as the foundation for the next development phase, described in Chapter 5, in which the conventional actuation mechanism is progressively replaced by HASEL-based soft actuation, while preserving the validated walker geometry.

Chapter 5

HASEL Actuator Integration

5.1 Actuator Selection and Characterization

Following the mechanical validation of the servo-actuated walker described in Chapter 4, attention was shifted toward integrating HASEL actuators as the primary actuation mechanism for the telescopic legs. The long-term objective is to evaluate whether soft electrohydraulic actuators can effectively drive a quasi-passive walking robot while simultaneously providing beneficial compliance and shock-absorption characteristics.

The actuator selected for this study was the E-0025-04-15 HASEL actuator, characterized by a maximum force of 40 N, a maximum unloaded displacement of 7 mm, dimensions of 54 mm diameter × 20 mm height, and a mass of 88 g. Both the actuator and the driving electronics were sourced from Artimus Robotics. The actuator was driven using a four-channel programmable high-voltage power supply from the same manufacturer, operated at a voltage of 6 kV, the manufacturer-recommended maximum operating voltage for this actuator model.



Figure 5.1: The E-0025-04-15 HASEL actuator used in this study. Actuator parameters according to the manufacturer (blocking force, free displacement, dimensions, weight) [3].

The load–displacement data used for actuator selection were taken from an internal characterization campaign carried out at the ETIS laboratory by Nayah Cornily on the same E-0025-04-15 actuator model available for this project [6]. The characterization compared a single actuator with two-actuator arrangements in parallel and in series. For the load-response tests, applied masses spanning

approximately 57 g to 4 kg were tested at 1, 3, and 6 kV using a 1 Hz square-wave command with a duty cycle of 0.5. Displacement was measured optically using an AR0330 camera operating at 24 fps, with a graduated ruler providing the spatial reference, and the measurements were processed through a Python-based tracking interface. Table 5.1 reports the 6 kV results, corresponding to the maximum operating voltage used in the present thesis. The reported mechanical work was computed from the applied load force and measured displacement as $W = F\,\Delta x = mg\,\Delta x$. These measurements are used here as reference input for actuator selection and transmission sizing; they were not independently repeated as part of the walker experiments in this thesis.

Table 5.1: HASEL actuator load–displacement characterization at 6 kV for single, parallel, and series actuator arrangements. Values are shown as displacement / mechanical work.

Load (g)	Single	Parallel	Series	Best performance
57	6.26 mm / 3.50 mJ	5.22 mm / 2.92 mJ	11.28 mm / 6.31 mJ	Series
210	5.52 mm / 11.37 mJ	7.01 mm / 14.45 mJ	10.15 mm / 20.91 mJ	Series (ampl.) / Parallel (work)
460	4.54 mm / 20.47 mJ	5.60 mm / 25.29 mJ	8.18 mm / 36.91 mJ	Series
638	4.06 mm / 25.38 mJ	3.74 mm / 23.41 mJ	6.40 mm / 40.06 mJ	Series (work)
1100	4.46 mm / 48.09 mJ	3.52 mm / 37.99 mJ	2.46 mm / 26.56 mJ	Single
2000	1.20 mm / 23.63 mJ	3.05 mm / 59.81 mJ	1.14 mm / 22.29 mJ	Parallel
3000	0.36 mm / 10.63 mJ	2.63 mm / 77.48 mJ	0.45 mm / 13.37 mJ	Parallel
4000	0.12 mm / 4.73 mJ	0.55 mm / 21.60 mJ	0.23 mm / 8.92 mJ	Parallel

Within the load range relevant to the walker (the complete robot was later measured at 862 g, including a 205 g battery, see Section 4.3), the displacement of a single actuator under load was found to be approximately 4–4.5 mm. This is not dramatically lower than the unloaded displacement of 7 mm, but it becomes problematic once combined with friction and compliance in the mechanical transmission. Previous walking experiments with the servo-driven prototype (Section 4.6) indicated an experimentally observed threshold of approximately 5 mm before a noticeable influence on gait dynamics could be observed, meaning the displacement

available from a directly-coupled actuator would likely be insufficient on its own to reliably drive the walking mechanism.

5.2 The HASEL–Mechanism Interface

Before any transmission mechanism could be designed, it was necessary to solve a more basic problem: the HASEL actuator itself is soft and deformable, and cannot be connected directly to a rigid robot structure using conventional mounting methods. A dedicated rigid interface was therefore designed from scratch, specifically for this project, to sit between the actuator and any downstream transmission mechanism.

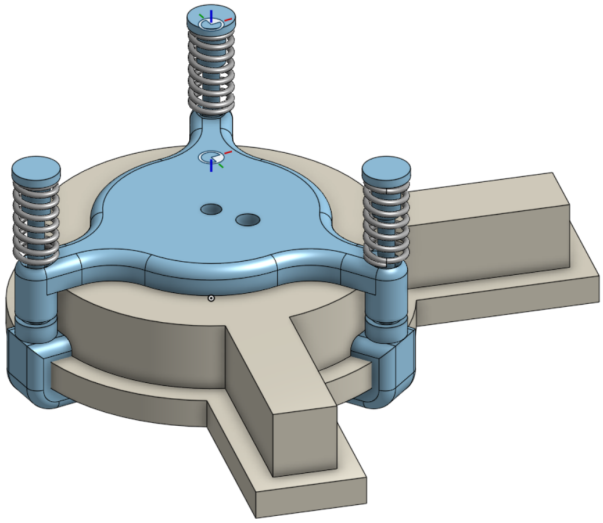


Figure 5.2: CAD render of the rigid HASEL–mechanism interface, showing the spring-loaded linear guides around the central actuator support.

The interface consists of a lower support in contact with the actuator, and an upper moving plate responsible for transferring the actuator's displacement onward to whichever transmission mechanism it is coupled to. To constrain the motion of the upper plate to a purely linear path, nails were used as low-friction linear guides: a simple, lightweight, and compact solution that avoids the higher friction of a less constrained sliding arrangement. Springs mounted around the guide nails, retained by spring caps, continuously push the upper plate down against the actuator surface, maintaining contact throughout the actuation cycle and providing a passive return toward the neutral position when the actuator is not energized.

The springs used were not ideal for this application: they were somewhat too stiff and too short to follow the actuator's full range of motion. A significant part of the

interface design effort went into calibrating the spring-cap geometry to balance two competing requirements: minimizing the preload resisting the actuator's motion, versus ensuring a sufficiently reliable return to the neutral position. Reducing preload improved freedom of motion but risked losing consistent contact with the actuator; increasing it improved reset reliability at the cost of added resistance to the actuator's stroke. This trade-off was only partially resolved with the springs available during the internship (see Section 5.5.3).

5.2.1 Modular Mechanical Connection

An important design objective of the interface was not only to transmit the actuator's displacement, but also to provide a *modular mechanical connection* that could be reused, unmodified, across the different design iterations of the project. Rather than designing a dedicated attachment for each transmission concept in turn, the upper moving plate was equipped with a standardized mounting interface that remained unchanged throughout the entire development process. This same modular connection was subsequently used for the direct-drive prototype (Section 5.3 below), the lever-based amplification mechanism (Section 5.4), and the later scissor-based transmission (Section 5.5), allowing each new transmission concept to be designed, manufactured, and tested independently, without having to redesign the actuator interface itself for every iteration.





Figure 5.3: The modular mounting interface: the standardized lower moving plate, with its central fastening screw and positioning pin, mounted on the 3D-printed leg (left); and the same connector in use, coupling the scissor-based transmission mechanism to the actuator interface (right). This connector geometry was reused unmodified across the direct-drive, lever-based, and scissor-based transmission mechanisms.

The connection consists of two functional elements: a central fastening screw and a positioning pin. The central screw prevents separation between the two connected components by constraining relative motion normal to the connection plane, effectively clamping the transmission mechanism against the interface plate. The positioning pin, offset from the central screw, prevents relative rotation between the interface and the attached transmission mechanism, so that the two parts can only be assembled in a single, repeatable orientation. Together, this two-point constraint (one linear, one rotational) provides a compact and mechanically robust coupling while still allowing rapid interchangeability between different transmission systems: disassembly and reassembly of a different mechanism onto the same actuator interface required removing and replacing only the central screw, with the positioning pin ensuring correct alignment was recovered automatically.

This modular philosophy considerably simplified the iterative design process described in the remainder of this chapter. Instead of redesigning the entire HASEL mounting assembly for every new prototype, only the transmission mechanism itself had to be modified, which meaningfully reduced design time, manufacturing effort, and assembly complexity across the three transmission architectures that were ultimately tested.

This interface was designed entirely from scratch. No directly comparable rigid

guiding and modular mounting interface was identified in the literature reviewed for this thesis. Designing this component was an essential enabling step for the practical integration of the actuator into any of the mechanical architectures explored in this chapter, and it is revisited as one of the more transferable contributions of this work in Section 5.5.3 and Chapter 6.

5.3 Direct-Drive Attempt

The simplest candidate architecture was a direct coupling between the actuator (via the interface of Section 5.2) and the telescopic leg mechanism, in which actuator displacement would generate the required leg motion without additional mechanical components. This offered a compact, lightweight, mechanically simple solution minimizing transmission losses. A first prototype concept was developed based on this direct-drive architecture and evaluated experimentally.

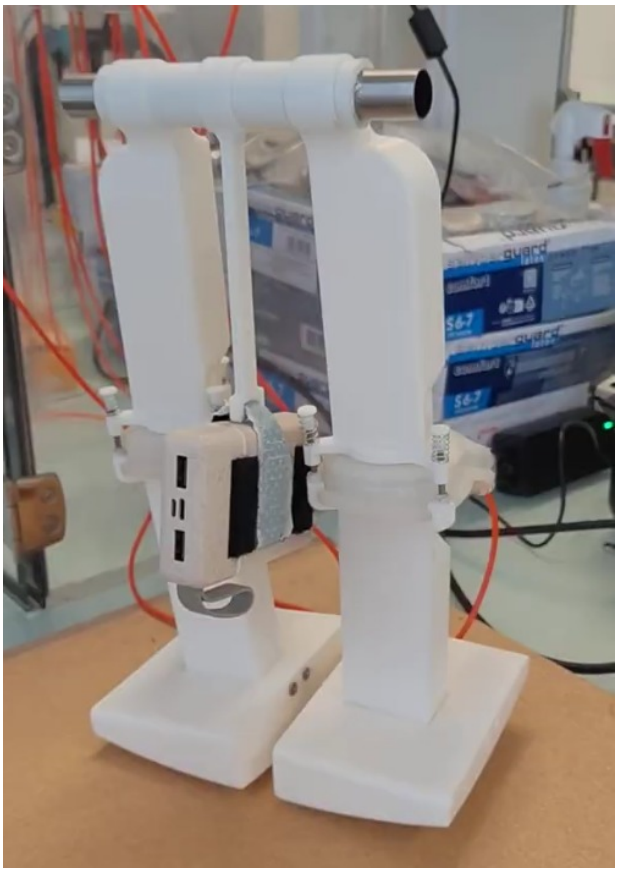


Figure 5.4: First direct-drive prototype coupling the HASEL actuator directly to the telescopic leg.

The evaluation revealed two limiting issues. First, as noted above, the available displacement under load (4–4.5 mm) was insufficient relative to the ∼5 mm minimum amplitude required to noticeably affect gait dynamics. Second, because the HASEL actuator is inherently compliant, directly integrating it into the structural load path of the leg caused the mechanism to become excessively flexible: instead of producing purely axial extension, part of the motion was absorbed through unwanted bending and deformation of the leg assembly, reducing displacement-transfer efficiency and introducing additional variability into the gait behavior. The direct-drive concept was therefore not a practical solution for the current walker architecture, motivating a transmission architecture that could both amplify the actuator's limited displacement and mechanically decouple the actuator's compliance from the leg's structural alignment.

5.4 Lever-Based Amplification Mechanism

A revised actuation architecture was developed combining a lever-based motion amplification mechanism with an integrated prismatic guide, designed as a single mechanical subsystem, mounted on the same modular interface described in Section 5.2. This mechanism was intended to amplify the HASEL actuator's displacement to a level compatible with the telescopic leg's extension requirements, while the prismatic guide constrained the motion to a single linear direction, preventing the actuator from introducing unwanted bending into the structure. Unlike the direct-drive configuration, the HASEL actuator would no longer be responsible for maintaining structural alignment: the mechanical structure would carry lateral and bending loads, while the actuator would contribute only axial displacement, retaining its beneficial compliance and damping properties without compromising the rigidity of the walker.

The lever geometry was designed to provide an amplification ratio slightly greater than 2:1, which, combined with the estimated 4–4.5 mm actuator displacement under load, was expected to yield approximately 8–9 mm of output displacement, comfortably above the approximately 5 mm displacement threshold observed in the preceding walker experiments.

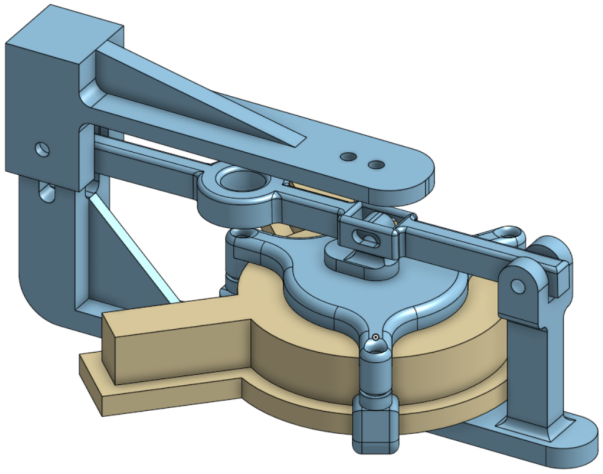


Figure 5.5: CAD design of the lever-based amplification mechanism with integrated prismatic guide.

A physical prototype of this lever-based mechanism was manufactured and tested. Although theoretically capable of providing the required displacement amplification, testing revealed a significant limitation in the positioning of the prismatic joint: the sliding guide was laterally offset from the main axis of the telescopic leg rather than positioned directly underneath and coaxially with it. As a consequence, the transmitted force did not act purely along the translation axis of the prismatic joint; the lateral offset generated an undesired moment on the slider, producing a parasitic torque that forced the sliding surfaces against the guide. The resulting friction was the dominant failure mode of the lever mechanism: under load, the joint could partially or completely bind, so much of the actuator motion was dissipated at the guide instead of being transmitted to the telescopic leg. This was particularly severe because the HASEL actuator already had little stroke and force margin, making even modest frictional losses mechanically decisive.

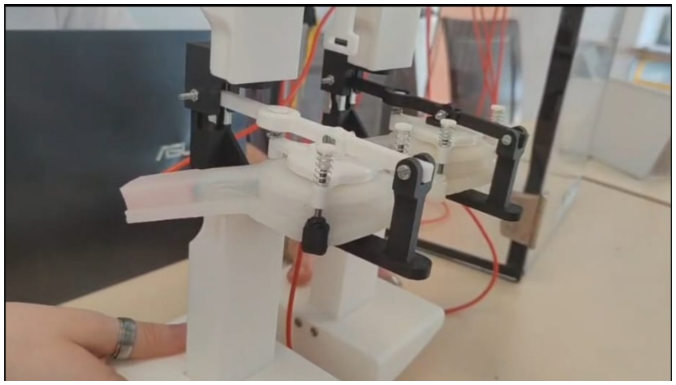


Figure 5.6: Physical prototype of the lever-based amplification mechanism under manual testing.

One possible solution would have been to redesign the lever and reposition the actuator farther from the leg axis to improve force alignment; however, this was considered undesirable, since the HASEL actuator represents a non-negligible mass, and moving it farther from the leg axis would alter the walker's mass distribution and potentially shift its center of mass. Given that the walker dynamics were shown in Chapter 4 to be highly sensitive to relatively small changes in mass distribution, and that one of the project's objectives is to preserve the mechanically validated walker geometry while replacing only the actuation system, a design requiring significant displacement of the actuator mass was judged unsuitable. Further development of the lever-based architecture was therefore discontinued in favor of an alternative transmission concept.

5.5 Scissor-Based Motion Amplification Mechanism

5.5.1 Design

To address the limitations identified in the lever-based prototype, a new transmission architecture was developed based on a pantograph-like scissor mechanism, aiming to preserve the required displacement amplification while keeping the HASEL actuator as close as possible to the main leg axis. In the proposed configuration, the actuator is positioned vertically and close to the leg structure; rather than acting directly along the telescopic extension axis, it applies its linear displacement laterally to the scissor mechanism, whose pantograph geometry redirects the input motion by approximately 90°, converting it into linear motion aligned with the telescopic leg. As with the lever mechanism, the selected geometry targets an

amplification ratio of approximately 2:1, intended to raise the estimated 4–4.5 mm actuator displacement to approximately 8–9 mm at the mechanism output.

A key advantage of this architecture is the positioning of the actuator mass: mounting the HASEL actuator vertically and close to the leg axis minimizes changes to the walker's existing mass distribution, which is particularly important given its experimentally demonstrated sensitivity to center-of-mass position. The scissor architecture also eliminates the laterally-offset prismatic guide responsible for the excessive friction observed in the lever prototype; however, it introduces multiple rotational joints and pivots, making joint friction an important design consideration in its own right.

To reduce friction and avoid direct PLA-on-PLA sliding contact, the prototype uses steel pins at all scissor joints and rotational pivots, so that the printed PLA components rotate around smooth metallic pin surfaces rather than against other printed components. This was expected to reduce friction, improve repeatability, and limit wear during cyclic operation, and to provide better dimensional consistency at the pivot points than fully printed joints, where surface roughness, layer orientation, and printing tolerances could otherwise significantly affect the motion.

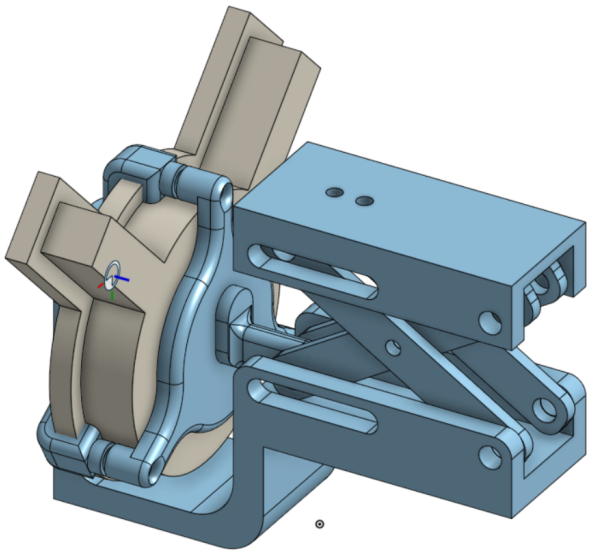


Figure 5.7: CAD design of the scissor-based (pantograph) amplification mechanism.

5.5.2 Tolerance Calibration and Lateral Guide

At least four physical iterations of the scissor mechanism were manufactured in order to identify suitable manufacturing tolerances and resolve a mechanical instability observed during testing.

The initial focus of this prototyping phase was calibrating the fit between the 3D-printed PLA scissor links and the steel pivot pins. Successive iterations were used to tune the clearance between the printed holes and the pin diameter: excessive clearance produced noticeable play and backlash at each joint, while insufficient clearance caused binding and increased friction. Both effects are particularly detrimental given the already-limited stroke available from the HASEL actuator.

After minimizing pivot tolerances to an acceptable level, a further and unexpected issue became apparent during actuation testing. Even with well-fitted pivots, the scissor mechanism exhibited a tendency to deflect laterally out of its intended plane of motion, rather than actuating purely along the designed extension axis. This lateral instability was traced to the asymmetry of the leg's spherical foot contact surface: because the foot geometry is not perfectly symmetric, the leg is subject to an uneven loading condition that introduces a bending moment into the structure. This moment is transmitted through the leg into the scissor mechanism, causing the scissor links to buckle sideways under load rather than remaining constrained to their intended linear actuation path.

To address this, a lateral guide was introduced to constrain the out-of-plane motion of the mechanism. The guide consists of an additional steel rod, matching the diameter used for the scissor pivot joints, mounted to run alongside the mechanism and physically prevent lateral deflection. To minimize the additional friction introduced by this new constraint, nylon washers were used at the sliding interface between the guide rod and the moving structure, since a nylon-on-steel contact provides low sliding friction compared to PLA-on-steel or PLA-on-PLA alternatives.



Figure 5.8: Assembled scissor mechanism showing the added lateral guide rod (steel, same diameter as the scissor pivot pins) and nylon washer used to constrain out-of-plane deflection while minimizing additional sliding friction.

5.5.3 Experimental Evaluation

The scissor mechanism, including the lateral guide, was evaluated in two stages: first stand-alone, decoupled from the leg and foot assembly, to verify its kinematic amplification ratio under controlled loading; second, integrated onto the complete walker, to evaluate whether it could produce useful locomotion when driven by the HASEL actuator.

Stand-alone mechanism performance. Tested independently, the scissor mechanism exhibited satisfactory mechanical behavior. The steel pins at the rotational joints reduced the friction associated with direct PLA-on-PLA contact, and the pantograph geometry successfully redirected the horizontal input displacement into an approximately vertical output displacement. A small experimental characterization was performed by applying different loads and measuring both the HASEL actuator's displacement and the corresponding mechanism output displacement.

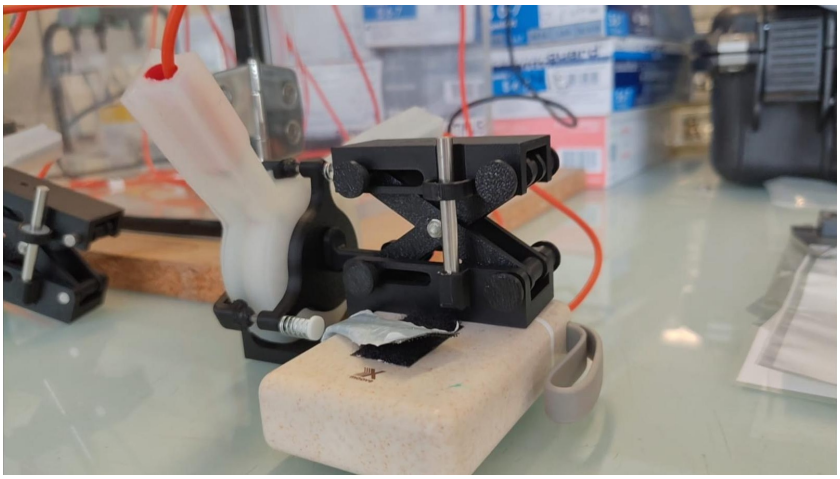


Figure 5.9: The scissor mechanism under stand-alone bench testing, used to measure the input/output displacement ratio under applied load.

Table 5.2: Stand-alone scissor mechanism: output linear displacement for increasing externally applied load.

External weight (g)	Linear displacement (mm)
0	6
5	5
50	5
500	4

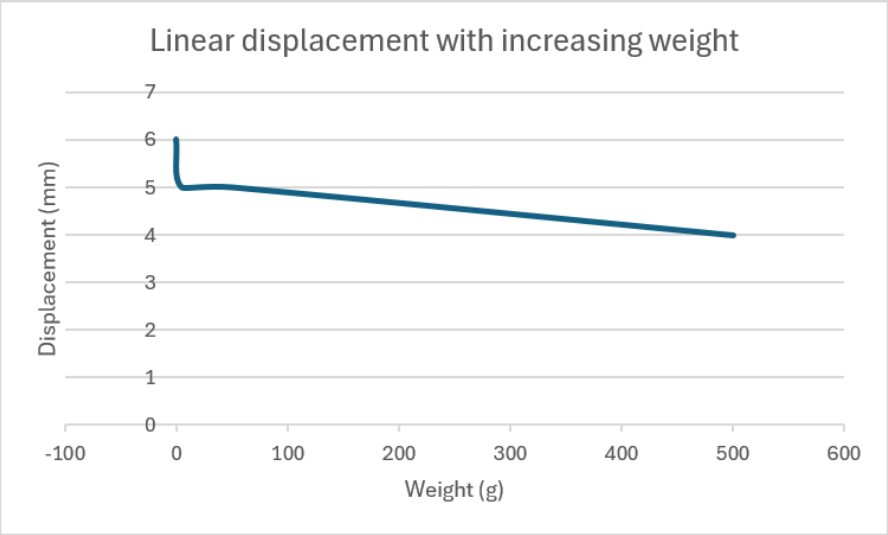


Figure 5.10: Output linear displacement of the stand-alone scissor mechanism as a function of applied load, corresponding to the data in Table 5.2.

The measurements confirmed the expected displacement amplification: in one representative test, an input displacement of approximately 3 mm at the actuator generated an output displacement of approximately 6 mm, experimentally validating the intended **2:1 amplification ratio**. This test should not be interpreted as a truly unloaded actuator measurement: even with no external weight applied, the return springs in the HASEL interface exerted a residual preload on the actuator. Because the available springs were slightly too stiff and too short, this preload reduced the available actuator stroke and contributed to the approximately 3 mm input observed in the representative test. The purpose of this measurement was therefore to validate the transmission ratio rather than the actuator's unloaded displacement. The spring-based return system also did not always return the upper interface plate fully to its neutral position after actuation. Despite iterative calibration of the spring-cap geometry, this limitation affected repeatability, though it did not invalidate the displacement amplification demonstrated by the isolated mechanism.

Integration into the complete walker. The mechanism's behavior changed significantly once installed on the complete walker. During walking, the telescopic legs do not experience purely axial loading: the spherical feet are wedge-shaped when viewed from the frontal plane, and this geometry intentionally produces the lateral rocking and alternating weight transfer that the walker's locomotion principle depends on. This lateral motion is essential: it is not a design flaw to be removed, but the mechanism by which the walker shifts weight from one leg to

the other, and it causes the legs to bend and rotate slightly during each gait cycle. As a result, the scissor mechanism and its output guide were subjected to bending moments and lateral forces they had not been designed to tolerate.

Although the nylon-on-steel lateral guide (Section 5.5.2) reduced friction under idealized, symmetric loading, the misalignment generated by real leg bending during stance forced the moving components against the guide surfaces regardless. The resulting lateral contact substantially increased friction and consumed a large fraction of the available actuator stroke before it could reach the telescopic leg. In practice, friction was therefore also the dominant mechanism-level failure mode of the scissor transmission once mounted on the walker. This is the same fundamental problem that had defeated the lever-based design (Section 5.4): both amplification mechanisms worked under controlled, approximately axial conditions, but off-axis loading generated contact forces and friction that prevented efficient motion transmission during real walking.

In the final full-robot test, the available leg displacement was too small to produce an effective gait: instead of walking forward, the robot mainly exhibited lateral wobbling in place. Part of the HASEL actuator's motion was lost through a combination of: friction in the lateral guide under load-induced misalignment; deformation of the printed components; bending of the telescopic leg itself; incomplete spring return within the actuator interface (Section 5.2); and mechanical play across the mechanism's multiple joints.

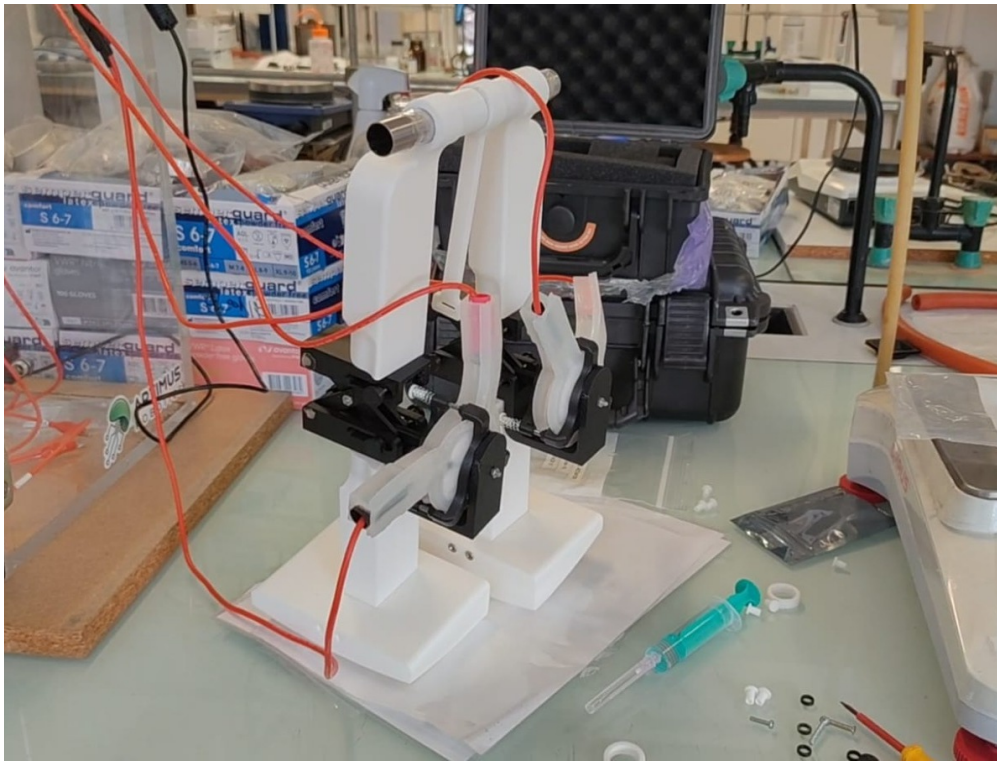


Figure 5.11: The scissor mechanism mounted in place on the walker legs.

5.5.4 Mechanical Interpretation

Critically, this failure cannot be resolved simply by redesigning the feet to produce purely axial leg loading. The spherical, laterally-offset foot geometry is precisely what generates the side-to-side oscillation required for weight transfer and forward walking in a quasi-passive design of this type (Chapter 4); eliminating this asymmetry would remove the very mechanism that makes the robot walk at all. The transmission mechanism must therefore be able to tolerate lateral bending and torsional loads while still delivering low-friction axial displacement, and achieving this using compact, 3D-printed components with multiple small pivots, driven by an actuator with as little force and stroke margin as HASEL provides, proved impractical within the scope of this work. A more rigid, all-metal mechanism with precision bearings and tighter alignment tolerances could plausibly reduce these losses, but such a solution would add mass, complexity, and stiffness, eroding several of the advantages that motivated considering HASEL actuation in the first place.

5.6 Summary

Across three successive transmission architectures, direct-drive, lever-based, and scissor-based, built around a common, purpose-designed rigid interface for coupling the soft HASEL actuator to rigid structure (Section 5.2), two distinct limitations emerged. The direct-drive concept was limited primarily by insufficient displacement and structural compliance. By contrast, the lever and scissor amplification mechanisms were both ultimately defeated by friction generated when non-axial loading forced their moving elements against guides or constrained joints. The walker's leg and foot geometry, essential to its passive-dynamic locomotion principle, unavoidably produces this off-axis loading during walking. Because the actuator has very limited stroke and force margin under load, these frictional losses consume a mechanically significant fraction of the available output. The scissor mechanism, the most refined of the three designs, delivered its intended 2:1 kinematic amplification in isolation, but that displacement did not survive once the real walker introduced bending, lateral contact, and the associated friction. This result, together with the reusable actuator interface developed along the way, is discussed further in Chapter 6.

Chapter 6

Discussion

6.1 From Rigid to Soft Actuation: What Carries Over

The servo-driven characterization of the walker (Chapter 4) established concrete experimental requirements for viable locomotion on this platform: an observed extension-amplitude threshold of approximately 5 mm before gait dynamics are noticeably affected, a best-performing tested actuation frequency around 1.0 Hz, and a strong sensitivity to mass distribution and foot-ground contact conditions. These requirements were used throughout Chapter 5 to evaluate whether a given HASEL transmission design could, in principle, deliver sufficient displacement.

The HASEL-driven result did not meet this threshold in practice. Although the scissor mechanism was shown, in isolation, to deliver its intended displacement (Section 5.5.3, approximately 3 mm in $\rightarrow$ 6 mm out under the residual preload of the return springs, confirming the 2:1 ratio), this displacement did not survive intact once the mechanism was integrated onto the real walker. The gap between isolated-mechanism performance and integrated-system performance is itself an important finding: it shows that characterizing a transmission mechanism on the bench, under idealized, symmetric loading, is not sufficient to predict its behavior once coupled to a real leg subject to the non-axial loading that the walker's own gait dynamics require.

6.2 Mechanical Lessons from Three Transmission Attempts

The direct-drive, lever-based, and scissor-based architectures form a coherent design-evolution narrative rather than three unrelated failures. Each iteration correctly diagnosed and addressed the specific failure mode of its predecessor: the direct-drive attempt's insufficient displacement and structural compliance motivated the lever's amplification and prismatic guide, while the lever's off-axis friction motivated the scissor's more coaxial, guided geometry. The scissor mechanism was

the mechanically soundest of the three and the only one confirmed to deliver its designed displacement ratio in isolation. However, the lever and scissor mechanisms were both ultimately defeated by the same mechanism-level effect: friction generated by off-axis loading. In the lever, a lateral guide offset created a parasitic moment and binding; in the scissor, stance-induced leg bending forced moving parts against the lateral guide and joints, again increasing contact friction and consuming the available stroke. The wedge-shaped spherical foot, which is precisely what allows the robot to rock side to side and transfer weight between legs, inherently produces this bending during stance. The key conflict is therefore that the gait requires non-axial loading, while both amplification mechanisms require low-friction, approximately axial motion to transmit the HASEL actuator's already limited output efficiently.

6.3 HASEL Feasibility for This Walker Design

Taken together, the results of Chapter 5 indicate that HASEL actuation, in its current form (E-0025-04-15, 40 N maximum force, 7 mm unloaded / 4–4.5 mm loaded displacement), is **not feasible as the primary actuator for this quasi-passive walker design**. The immediate mechanical cause that defeated both amplification mechanisms was friction induced by non-axial loading: the lever bound in its offset prismatic guide, while the scissor lost displacement when leg bending forced its guided elements into lateral contact. The actuator's limited force and displacement margins made these frictional losses decisive, because there was insufficient reserve to overcome them while still delivering the required leg extension. Since the non-axial loading is intrinsic to the walker's gait principle rather than an artifact of a single transmission design, solving the problem would likely require a locomotion architecture designed around the actuator's constraints from the outset rather than another retrofit transmission.

6.4 The HASEL Interface as a Reusable Contribution

While the walker-level integration did not succeed, the project's most transferable outcome is arguably the rigid actuator interface developed in Section 5.2: a linear-guided, spring-loaded mount that stabilizes the compliant HASEL actuator inside a rigid structure, maintains continuous contact with it, provides a passive return function, and offers a modular attachment point compatible with multiple downstream mechanisms. It was reused, unmodified, across the direct-drive, lever, and scissor architectures. No directly comparable design was identified in the literature reviewed for this thesis, suggesting that the interface may represent a useful transferable contribution independent of the walker application. With

improved springs, longer-travel and less stiff, so as to properly cover the actuator's full range of motion, this interface could provide a reliable, general-purpose way of converting HASEL deformation into homogeneous, parallel linear motion for other projects.

6.5 Implications for HASEL Applications

The experience gained across all three transmission attempts suggests a more general conclusion about where this class of HASEL actuator is practically useful. Its limited force and stroke margin, combined with its sensitivity to any off-axis loading, make it poorly suited to applications like this one, which demand large cyclic strokes transmitted through a mechanically complex amplification system embedded in a dynamic, non-axially-loaded structure. It appears much better suited to small, direct-drive corrective motions in applications where loading remains close to axial and the required displacement is modest, for example fine positioning, preload or tension adjustment, and small compliant posture corrections. These roles are closer to the kind of fine, stabilizing adjustment envisioned in the original bio-inspired balancing-joint concept described in Chapter 1, rather than the primary, large-stroke drive for a full locomotion mechanism.

6.6 Answering the Research Questions

Regarding the mechanical constraints governing HASEL integration into a quasi-passive walker, this thesis identifies the actuator's limited force and stroke margin under load as the binding constraint, and shows that this margin is easily consumed by non-axial loading that is intrinsic to the walker's own locomotion principle, not merely an artifact of a particular leg or transmission design.

Regarding which transmission architectures are best, or least poorly, suited to this coupling problem, of the three tested, the scissor-based, coaxially-guided design was the most mechanically sound and correctly amplified displacement in isolation. However, both the lever and scissor mechanisms failed once non-axial gait loading generated enough friction and binding to consume the available actuator displacement; the direct-drive concept failed earlier because of insufficient stroke and excessive structural compliance.

Regarding the class of applications this type of HASEL actuator is practically suited to, the evidence from this thesis points away from large-stroke, dynamically-loaded mechanisms such as legged locomotion, and toward small, direct-drive corrective or fine-positioning applications where loading can be kept close to axial.

Chapter 7

Conclusion and Future Work

7.1 Conclusion

This thesis set out to investigate the practical integration of HASEL soft actuators into a quasi-passive walking robot, building on a mechanically validated, servo-driven walker platform and preceded by a preliminary, exploratory phase of compliant-control experiments on the SO-101 robotic arm.

A quasi-passive walker was designed from scratch, mechanically iterated, and characterized under conventional servo actuation, establishing a validated baseline and quantitative gait requirements (an observed displacement threshold of $\sim$5 mm and a best-performing tested actuation frequency of $\sim$1.0 Hz). Integrating a HASEL actuator into this platform first required designing a dedicated rigid interface capable of stabilizing the compliant actuator within a rigid structure while transmitting its motion linearly. No directly comparable design was identified in the literature reviewed for this thesis, and the interface is considered one of the more broadly useful outcomes of this work. Three successive transmission architectures were then designed and tested: direct-drive, lever-based, and scissor-based. The direct-drive concept was limited by insufficient displacement and structural compliance. The lever and scissor mechanisms introduced motion amplification, but both were ultimately defeated by friction generated under non-axial loading. In the lever, guide misalignment produced a parasitic moment and binding; in the scissor, the mechanism achieved its intended 2:1 amplification in isolation (approximately 3 mm input producing 6 mm output under residual return-spring preload), but real gait-induced leg bending forced the guided components into lateral contact, increasing friction and consuming the available displacement. The assembled HASEL-driven robot therefore did not walk and produced only an in-place wobbling motion.

The overall conclusion of this work is that HASEL actuation, in its current characterized form, is **not a practical primary actuator for this quasi-passive walker architecture**. The decisive limitation is the combination of unavoidable non-axial gait loading and the actuator's very limited force and stroke margin. The non-axial loading creates friction in guided amplification mechanisms, as observed independently in both the lever and scissor designs, while the actuator provides

too little reserve to overcome those losses and still deliver sufficient leg extension. This is still a legitimate and useful engineering conclusion: it identifies not only that the integration failed, but the physical mechanism responsible for the failure and the boundary conditions under which it occurred. The results point toward small, direct-drive, close-to-axial corrective motions as a better fit for this HASEL actuator than large-stroke, dynamically-loaded locomotion mechanisms.

7.2 Limitations

The experimental scope of this thesis is limited in several respects. The preliminary SO-101 arm experiments (Chapter 3) controlled a single joint at a time and did not feed directly into the walker's design. The walker's servo-driven characterization (Chapter 4) used open-loop actuation and a qualitative 1–4 gait scoring system rather than fully quantitative gait metrics; the velocity characterization was also based on only one or two 2 m runs per operating point and should therefore be interpreted as exploratory rather than as a repeatability study. The HASEL load–displacement data used for actuator selection (Table 5.1) were taken from a prior internal laboratory characterization [6] rather than independently replicated within this project. The HASEL integration work itself (Chapter 5) was constrained by the time available at the end of the internship: the stand-alone scissor mechanism characterization (Table 5.2) reflects a small number of trials, and the underperforming spring return was identified but not resolved with an alternative spring within the project timeline.

7.3 Future Work

- **Refine and reuse the actuator interface with better springs.** The interface developed in Section 5.2 (linear-guided, spring-loaded, modular mount) worked well in principle. Replacing its springs with longer-travel, lower-stiffness components, so that the actuator's full stroke is covered with lower preload, would likely make it a reliable, general-purpose building block for future HASEL-based projects, independent of the walker application.
- **Target small, direct-drive applications for this HASEL actuator type**, such as fine positioning, tension/preload adjustment, or small compliant posture corrections, rather than large-stroke locomotion. These are closer to the original bio-inspired balancing-joint concept described in Chapter 1, where HASEL actuators act as fine adjustment elements rather than primary drivers of motion.

- **If HASEL-driven legged locomotion is pursued further**, treat it as a from-scratch locomotion architecture problem rather than a retrofit: design the leg/foot/gait principle around the actuator's force and stroke constraints from the outset, rather than adapting a mechanism whose passive dynamics were established around a stiffer, higher-force servo.
- **Quantify scissor-joint friction and backlash directly**, for example via torque or force measurement at the actuator input under controlled off-axis loading, to build a predictive model of how much displacement a given transmission design will lose once subjected to a known bending moment, rather than relying on integrated full-robot testing to discover this empirically.
- **Multi-joint coordination and closed-loop control**, extending the single-joint stabilization experiments of the preliminary SO-101 work (Chapter 3) toward full-body bio-inspired balance control, as originally outlined in the inverted-pendulum setup of Section 3.8. This is a separate line of work from the walker, but one that could eventually make use of the apparent-compliance strategies explored there.

Appendix A

Control Software Listings

Listing A.1 reports the complete Arduino sketch used to generate the final, open-loop walking gait described in Section 4.3 and referenced in Section 4.6: two servo channels are driven by sinusoidal position commands, phase-shifted by 180° relative to one another, with the oscillation frequency, amplitude, and per-leg neutral (center) angle all exposed as simple tunable constants at the top of the file.

```
#include <Servo.h>
#include <math.h>

Servo servo1;
Servo servo2;

// -------- TUNE THESE --------
const int pin1 = 3;
const int pin2 = 4;

const float center1 = 75.0;   // neutral angle servo 1
const float center2 = 98.0;   // neutral angle servo 2

const float ampDeg = 13;      // start small: 8 to 15 deg
const float freqHz = 1.1;     // start slow
const int updateMs = 20;      // smaller = smoother updates
// ----------------------------

float t = 0.0;

void setup() {
  servo1.attach(pin1);
  servo2.attach(pin2);

  servo1.write(center1);
  servo2.write(center2);

  delay(1000);
}

void loop() {
  float w = 2.0 * PI * freqHz;
```

```
33
34    float s1 = sin(w * t);
35    float s2 = sin(w * t + PI);   // 180 degrees out of phase
36
37    int a1 = (int)(center1 + ampDeg * s1);
38    int a2 = (int)(center2 - ampDeg * s2);
39
40    servo1.write(a1);
41    servo2.write(a2);
42
43    t = t + (updateMs / 1000.0);
44    delay(updateMs);
45  }
```

Listing A.1: Arduino sketch generating the final open-loop, phase-shifted sinusoidal walking gait.

Listing A.2 reports the Arduino sketch used to acquire raw accelerometer and gyroscope readings from the MPU-6050 over I2C and stream them over serial, timestamped, for the calibration procedure described in Section 3 and the postural stabilization experiments that follow it: the sketch also computes a simple single-axis tilt angle from the accelerometer reading (via `atan2`) and an angular velocity from the gyroscope reading, as a first, minimal orientation estimate ahead of the fuller calibration and low-pass filtering procedure described in the main text.

```
1  #include <Wire.h>
2  #include <MPU6050.h>
3  #include <math.h>
4
5  MPU6050 mpu;
6
7  void setup() {
8    Serial.begin(115200);
9    Wire.begin();
10   mpu.initialize();
11 }
12
13 void loop() {
14   int16_t ax, ay, az, gx, gy, gz;
15   mpu.getMotion6(&ax, &ay, &az, &gx, &gy, &gz);
16
17   float angle = atan2((float)ax, (float)az) * 180.0 / PI;
18   float angular_velocity = gx / 131.0;
19
20   Serial.print(millis());
21   Serial.print(",");
22   Serial.print(ax);
23   Serial.print(",");
24   Serial.print(ay);
```

```
25    Serial.print(",");
26    Serial.print(az);
27    Serial.print(",");
28    Serial.print(gx);
29    Serial.print(",");
30    Serial.print(gy);
31    Serial.print(",");
32    Serial.println(gz);
33
34    delay(10);
35  }
```

Listing A.2: Arduino sketch for raw MPU-6050 IMU acquisition and streaming.

Listing A.3 reports the core control loop of the IMU + effort-based elbow compliance experiment (Section 3); serial communication, IMU-thread management, and the initial calibration of the reference pitch and effort bias are omitted for brevity, following the same structure as Listing A.2.

```
1  # Tunable gains and limits
2  K_PITCH_POS = 0.020
3  PITCH_DEADBAND_DEG = 0.5
4  MAX_IMU_OFFSET = 0.55
5
6  EFFORT_THRESHOLD = 2
7  K_EFFORT = 0.008
8  MAX_EFFORT_OFFSET = 0.30
9
10 MAX_STEP_PER_CYCLE = 0.010  # rate limiting
11
12 # --- IMU position term ---
13 pitch_err = pitch_deg - pitch_ref
14 if abs(pitch_err) < PITCH_DEADBAND_DEG:
15     pitch_err = 0.0
16
17 imu_offset = K_PITCH_POS * pitch_err
18 imu_offset = clip(imu_offset, -MAX_IMU_OFFSET, MAX_IMU_OFFSET)
19
20 # --- Effort term ---
21 effort = effort_raw - effort_bias
22 effort_offset = 0.0
23 if abs(effort) > EFFORT_THRESHOLD:
24     effort_offset = sign(effort) * K_EFFORT * (abs(effort) -
   EFFORT_THRESHOLD)
25     effort_offset = clip(effort_offset, -MAX_EFFORT_OFFSET,
   MAX_EFFORT_OFFSET)
26
27 # --- Combined target, with rate limiting ---
28 elbow_target = q_start + imu_offset + effort_offset
29 elbow_target = clip(elbow_target,
```

```
30                          q_start - MAX_IMU_OFFSET,
31                          q_start + MAX_IMU_OFFSET)
32
33 q_cmd = move_toward(q_cmd, elbow_target, max_step=
       MAX_STEP_PER_CYCLE)
```

Listing A.3: Core control loop of the IMU + effort-based elbow compliance law (calibration, threading, and I/O omitted for brevity).

Bibliography

[1] Eric Acome, Shane K. Mitchell, T. G. Morrissey, M. B. Emmett, Christoph Benjamin, Madeline King, Miles Radakovitz, and Christoph Keplinger. Hydraulically amplified self-healing electrostatic actuators with muscle-like performance. *Science*, 359(6371):61–65, 2018. doi: 10.1126/science.aao6139.

[2] Arduino. *Arduino Mega 2560 Rev3 User Manual*. Arduino, 2026. URL `https://docs.arduino.cc/resources/datasheets/A000067-datasheet.pdf`. Accessed: 2026-08-17.

[3] Artimus Robotics. Expanding HASEL actuators. `https://www.artimusrobotics.com/expanding-actuators`, 2026. Accessed: 2026-08-16.

[4] Pranav A. Bhounsule, Jason Cortell, and Andy Ruina. Design and control of ranger: An energy-efficient, dynamic walking robot. In *Adaptive Mobile Robotics*, pages 441–448. World Scientific, 2012. doi: 10.1142/9789814415958_0057.

[5] Box2AI Robotics. LeRobot-Kinematics: Forward and inverse kinematics for the lerobot so-100/so-101 arm. `https://github.com/box2ai-robotics/lerobot-kinematics`, 2025. GitHub repository. Accessed: 2026-08-17.

[6] Nayah Cornily. Caractérisation HASEL. Internal technical report, ETIS Laboratory, CY Cergy Paris Université, May 2026.

[7] FEETECH RC Model Co., Ltd. FR0115M 6V 15 kg.cm Digital Robot Servo – technical specifications. Manufacturer product specification, 2026. URL `https://www.feetech.cn/6v-15kg-digital-robot-steering-gear_52307.html`. Accessed: 2026-09-21.

[8] Tom E. Flemons. The geometry of anatomy – the bones of tensegrity. `https://intensiondesigns.ca/geometry-of-anatomy/`, 2006. Accessed: 2026-08-16.

[9] David V. Gealy, Stephen McKinley, Brent Yi, Philipp Wu, Phillip R. Downey, Greg Balke, Allan Zhao, Menglong Guo, Rachel Thomasson, Anthony Sinclair, Peter Cuellar, Zoe McCarthy, and Pieter Abbeel. Quasi-direct drive for low-cost compliant robotic manipulation. In *2019 International Conference on Robotics and Automation (ICRA)*, 2019. doi: 10.1109/ICRA.2019.8794236.

[10] Neville Hogan. Impedance control: An approach to manipulation: Part I—theory. *Journal of Dynamic Systems, Measurement, and Control*, 107(1):1–7, 1985. doi: 10.1115/1.3140702.

[11] Hugging Face. SO-101: Assembly and setup guide. `https://huggingface.co/docs/lerobot/so101`, 2026. LeRobot documentation. Accessed: 2026-08-16.

[12] InvenSense Inc. *MPU-6000 and MPU-6050 Product Specification*. InvenSense Inc., revision 3.4 edition, 2013. URL `https://product.tdk.com/system/files/dam/doc/product/sensor/mortion-inertial/imu/data_sheet/mpu-6000-datasheet1.pdf`. Accessed: 2026-08-17.

[13] Sharfin Islam, Kamal Carter, Justin Yim, James Kyle, Sarah Bergbreiter, and Aaron M. Johnson. Scalable minimally actuated leg extension bipedal walker based on 3D passive dynamics. In *2022 IEEE International Conference on Robotics and Automation (ICRA)*, pages 207–213, Philadelphia, PA, May 2022. doi: 10.1109/ICRA46639.2022.9812053.

[14] Tad McGeer. Passive dynamic walking. *The International Journal of Robotics Research*, 9(2):62–82, 1990. doi: 10.1177/027836499000900206.

[15] Artem Melnyk and Alexandre Pitti. Synergistic control of a multi-segments vertebral column robot based on tensegrity for postural balance. *Advanced Robotics*, 32(15):850–864, 2018. doi: 10.1080/01691864.2018.1483209.

[16] Open Robotics. ROS 2 Humble Hawksbill Documentation. `https://docs.ros.org/en/humble/`, 2022. Accessed: 2026-08-17.

[17] Gill A. Pratt and Matthew M. Williamson. Series elastic actuators. In *Proceedings 1995 IEEE/RSJ International Conference on Intelligent Robots and Systems (IROS)*, volume 1, pages 399–406, 1995. doi: 10.1109/IROS.1995.525827.

[18] Philipp Rothemund, Nicholas Kellaris, Shane K. Mitchell, Eric Acome, and Christoph Keplinger. HASEL artificial muscles for a new generation of lifelike robots—recent progress and future opportunities. *Advanced Materials*, 33(19):2003375, 2021. doi: 10.1002/adma.202003375.

[19] ServoDatabase.com. Feetech sts3215 standard servo specs. `https://servodatabase.com/servo/feetech/sts3215`, 2026. Accessed: 2026-08-17.